Nanomedicine

Cellulose Nanocrystals: a multimodal tool to enhance the targeted drug delivery against bones

Journal:	*Nanomedicine*
Manuscript ID	NNM-2020-0139.R1
Manuscript Type:	Research Article
Keywords:	Cellulose Nanocrystals, Drug Delivery System, Surface Functionalization, Bone Tropism

ABSTRACT

Aim: Herein, we investigated the use of Cellulose Nanocrystals (CNCs) as drug nanocarriers combining an anti-osteoporotic agent, alendronate (ALN), and an anti-cancer drug, doxorubicin (DOX). **Materials & methods:** CNC physicochemical characterization, *in vivo* imaging coupled with histology, *in vitro* uptake and toxicity assays were carried out. **Results:** *In vivo* CNC-ALN did not modify bone tropism and lung penetration, whereas its liver and kidneys accumulation resulted slightly higher compared to CNCs alone. *In vitro* studies showed that CNC-ALN did not impair the ALN effect on osteoclasts, while CNC-DOX confirmed the therapeutic potential against bone metastatic cancer cells. **Conclusions:** This study provides robust proofs about the potential of CNCs as easy, flexible and specific carriers to deliver compounds to the bone.

KEYWORDS

Cellulose Nanocrystals, Drug Delivery System, Surface Functionalization, Bone Tropism.

Introduction

One of the main challenges of pharmacological research is to develop or optimize targeted delivery systems to make systemic drug administration safer and more effective. With this aim, in the last two decades, different strategies have been investigated to deliver drugs by linking a targeting or penetrating agent to the therapeutic compound. Many of these systems, such as viral vectors, antibodies, peptides and liposomal formulations are already available for patients, while others are still under preclinical evaluation, including nanocarriers [1]. Nanocarriers have major advantages since they can load a great number of therapeutic agents and modulate their release, increasing the stability and reducing the off-target delivery. Nanocarriers can be "multitasking", enclosing targeting moieties, contrast agents or other compounds able to control the drug release depending on specific environmental conditions (e.g. pH, redox state, ionic composition) [2]. Moreover, slight modifications of physicochemical characteristics of nanoparticles, such as size, shape, surface charge, and coatings, can be exploited to modulate their interaction with the host [3]. In this context, it has been recently claimed that an overall characterization of bio-nano interaction should be carried out in the process of nanoparticle development in biomedicine [4].

Despite several decades of progress, bone-specific delivery is still limited by the unique anatomical features of bone. A practical solution is to produce targeted drugs with high affinity for hydroxyapatite [5]. Among the broad range of materials tested in the last decades, Cellulose NanoCrystals (CNCs), obtained from cellulose in a defect-free rod-like crystalline state, have attractive properties including high surface area, low density and good mechanical strength [6]. Our previous data demonstrated that CNCs show a high tropism toward bones, with low accumulation in filter organs and fast excretion, without detrimental effects both *in vivo* and *in vitro* [7]. Starting from these promising results, in the present study, we built-up CNCs linked with two different compounds, sodium alendronate (ALN) or doxorubicin (DOX), known for their efficacy to counteract the osteoporotic bone demineralization and to limit the metastatic spread of breast cancer cells to bone, respectively [8,9]. Despite their proven efficacy, both these drugs cause side effects

due to their off-target organ accumulation [10–13]. To overcome this limitation, we optimized the linkage of ALN to CNCs through an amide bond exploiting the carboxylic acid function introduced to CNC surface through an oxidation reaction. The loading of DOX was instead achieved through direct adsorption on CNC-SO_3^-. These new formulations were extensively characterized in terms of chemistry, morphology and drug release. Since a slight change in the nanocarrier structure can modify its tropism, we compared the biodistribution of CNC-SO_3^- and CNC-ALN after systemic injection in healthy mice. Finally, the ability to penetrate filter (macrophages) and target cells (osteoclasts for ALN and breast cancer cell line for DOX) were assessed.

Materials & Methods

CNC extraction

CNCs were extracted from Whatman#1 filter paper (Sigma-Aldrich) by acid hydrolysis according to a previously reported procedure [14]. In particular, 10 g of filter paper were treated with 64% H_2SO_4 for 1 h at 55°C with an acid/cellulose ratio of 10 w/w. After acidic treatment, the content of the flask was poured into a 10-fold volume of cold water and stirred. Cellulose sediment was purified by repeated centrifugations at 3200 g for 15 min, and the solid component was suspended in distilled water by ultrasonic mixing for 5 min. Then, the suspension was dialyzed against ultrapure Milli-Q water for 1 week until reaching pH 6. CNC-SO_3^- were recovered in about 40% yield, giving 400 ml of suspension at 1% w/V concentration.

CNC-ALN synthesis

The synthesis was accomplished following the procedure already reported in literature. Briefly, CNCs were submitted to a TEMPO (2,2,6,6-tetramethylpiperidine-1-oxyl radical, Sigma-Aldrich) mediated oxidation [15,16]. CNC-TEMPO were obtained at 50% yield, at a final concentration of 0.5% w/V. The synthesis of ALN-conjugated CNCs was carried out to 10 ml of 0.5% w/V CNC-TEMPO suspension (available carboxylic acid content: 0.92 mmol/g, titration). 1-ethyl-3-(3-dimethylaminopropyl) carbodiimide (EDC, 0.23 mmol, 191.7 g/mol) (Fluka Analytical) and N-

hydroxysuccinimide (NHS, 0.23 mmol, 115.1 g/mol) (Sigma Aldrich) were weighed in 5-fold molar excess, dissolved in 1 ml of bidistilled water, then added to the CNC suspension under stirring. After 1 h, a 5-fold molar excess of Sodium Alendronate (0.23 mmol, 325.1 g/mol) (Sigma-Aldrich) was added, the pH adjusted to 6.3-6.5 by adding 0.1 M phosphate buffer saline (Lonza), and the mixture was left to react overnight at RT. Purification of CNC-ALN was achieved through precipitation in EtOH/phosphate buffer solution (4:1), centrifugation (3200 g, 15 min, 2 cycles), redispersion in 10 ml and final dialysis against ultrapure Milli-Q water for 72 h using tubes in cellulose membrane with a molecular weight cut-off of 12000 Da (Sigma-Aldrich).

CNC-DOX synthesis

Adsorption of doxorubicin hydrochloride (Sigma-Aldrich) was performed at different loadings, according to the following CNCs/DOX ratios: 10:1, 4:1 and 2:1. To a set of CNC aqueous suspension (10 ml, 0.5% w/V, 50 mg), 5 µl of triethylamine (Et_3N) and 5.0, 12.5 and 25 mg of DOX were added, respectively. The suspensions were stirred at RT for 24 h. The sample purification was attained through successive CNC-DOX precipitation in EtOH and centrifugation cycles (3200 g, 15 min). The pellets were re-suspended restoring a 0.5% w/V concentration and dialyzed against distilled water for 72 h. Blank experiments without Et_3N were also performed under the same conditions. The amount of DOX adsorbed onto the CNC surface was assessed by UV-Vis analysis, according to the method described by Jackson JK et al. [17], using a DOX calibration curve, measured at 480 nm, described by the equation: $y = 19.302x + 0.0109$ ($R^2 = 0.9991$).

Alexa Fluor 633 labelled CNCs

To a suspension of CNCs (0.5%, 25 ml), 1 mg of Alexa Fluor 633 hydrazide, bis(triethylammonium) salt (Life Technologies), and 200 µl of acetic acid were added. The mixture was let to react at RT in the dark. After 24 h, the mixture was dialyzed against distilled water for 1 week to remove the acetic acid and the non-reactive fluorophore [7].

CNC characterization

The ATR-FTIR spectra were performed with a Nicolet iS10 spectrometer (Thermo Scientific) equipped with an iTR Smart device (total scan 32, range 4000-800 cm^{-1}, resolution 2 cm^{-1}). The UV-Vis absorption spectra were collected with a UV-Vis spectrophotometer Evolution 300 (Thermo Scientific). ^{31}P-NMR spectra were recorded on 800 µl of sample in deuterated water, D_2O, with 1 µl of trimethylphosphate as internal standard and with 20 mg of CNCs-ALN by a Bruker Advance 500 MHz instrument at RT. Relaxation delay of 5 s was used between scans (90° pulse angle). Line broadening of 3 Hz was applied to FIDs before Fourier transform. For each spectrum, typically 1000 scans were accumulated. For AFM analysis, 50 µl of CNCs were immediately added onto freshly cleaved mica for 5 min, then washed and dried under nitrogen flow. AFM analysis was carried out on a Multimode AFM with a Nanoscope V system (Veeco/Digital Instruments, Mannheim, Germany) operating in tapping mode, using standard antimony (n) doped silicon probes (T, 3.5-4.5 µm; L, 115-135 µm; K, 20-80 N/m) (Bruker Corporation, Billerica, MA). Images were acquired in height and amplitude error and analyzed by Scanning Probe Image Processor (SPIP-version-5.1.6) data analysis package (five different, well-separated areas). DLS and ζ-potential measurements were performed using a Zeta Sizer Nano 3600 (Malvern) with an operating laser (λ=632.8 nm) and a backscattering angle of 173°. The data were processed by Zetasizer Software 7.03. The samples were prepared by diluting initial particles of stock solution 0.5% w/V in Milli-Q water to obtain a final concentration of 140 mg/L. Measurements were carried out at 25°C using a disposable cuvette. Three replicate measurements per sample were performed to establish measurement repeatability.

Release of DOX from CNCs at acidic pH

The release of drug from DOX-loaded CNCs was performed according to the following procedure: for each sample described above (CNCs/DOX ratio 10:1, 4:1 and 2:1), a set of 3 vials containing 1 ml of CNCs-DOX suspension and 4 ml of acetate buffer (pH 5.1, 0.05 M) was placed in a water bath set at 45°C and kept under magnetic stirring for 6, 24 and 48 h, respectively. Then, excess EtOH was added to the suspension to precipitate CNCs. After centrifugation (3200 g, 10 min), the

supernatant containing the released DOX was recovered, the solvent rotary evaporated and then the dried solid residue dissolved in 1 ml of a 1:1 H_2O/EtOH solution. The obtained solutions, further diluted by the 1:1 H_2O/EtOH solution, when necessary, were finally subjected to UV-Vis analysis to measure the amount of released DOX.

Animals

The Institute for Pharmacological Research "Mario Negri"-IRCCS adheres to the principles set out in the following laws, regulations, and policies governing the care and use of laboratory animals: Italian Governing Law (D.lgs 26/2014; Authorization n.19/2008-A issued March 6, 2008 by Ministry of Health); Mario Negri Institutional Regulations and Policies providing internal authorization for persons conducting animal experiments (Quality Management System Certificate – UNI EN ISO 9001:2015 – Reg. N°6121); the NIH Guide for the Care and Use of Laboratory Animals (2011 edition) and EU directives and guidelines (EEC Council Directive 2010/63/UE). The Statement of Compliance (Assurance) with the Public Health Service (PHS) Policy on Human Care and Use of Laboratory Animals has been recently reviewed (9/9/2014) and will expire on September 30, 2019 (Animal Welfare Assurance #A5023-01). This work was reviewed by IRCCS-IRFMN Animal Care and Use Committee (IACUC) and approved by the Italian "Istituto Superiore di Sanità" (code: 42/2016-PR). Mice were maintained under specific pathogen-free conditions at the Institute's Animal Care Facilities. They received food and water *ad libitum* and were regularly checked by a certified veterinarian who is responsible for animal welfare supervision and experimental protocol revision.

Treatment and optical imaging

In the biodistribution studies, 45 CD1 female mice (30 g) were enrolled. Animals were treated with CNC-SO_3^- (n=20), CNC-ALN (n=20) and saline for the vehicle group (n=5). For each CNC formulation, animals were randomly sacrificed at 4, 24, 48 and 96 h (n=5 for each time-point). Mice were intravenously injected with 20 mg/kg of CNC-SO_3^- or CNC-ALN. Fluorescence images were acquired *in vivo* and *ex vivo* with IVIS Lumina III imaging system combined to X-rays scanning

(Perkin Elmer). The acquisition parameters were: excitation filter range: 680 to 740 nm, emission filter: 790 nm. Spectral unmixing and image analysis were performed using Living Image 4.3.1 software. After the last *in vivo* scanning, animals were sacrificed by an overdose of ketamine (150 mg/kg) and medetomidine (2 mg/kg). Liver, kidneys, spleen, lungs, vertebral column, and hind legs were explanted for *ex vivo* imaging.

Histology

Cryostat sections from livers, kidneys and lungs of mice sacrificed at 4 and 96 h after treatment, were cut at 20 µm. The Hoechst-33258 (2 µg/ml in PBS, Molecular Probes) was used to label nuclei, whereas CNCs were detectable for the presence of Alexa Fluor 633. The sections were analyzed by Olympus Fluoview microscope with confocal system FV500 equipped with specific lasers λ_{exc} 405 nm for Hoechst-33258 and λ_{exc} 635 nm to visualize the signal associated with CNCs. The post-processing of images was carried out through Image J software. Lungs from animals sacrificed at 96 h after treatment (n=2 for each group) were fixed in 10% neutral buffered formalin (Bio-Optica) for 24 h, paraffin-embedded and sectioned at 4 µm thickness. Haematoxylin-Eosin staining (H&E) was carried out and sections were visualized through a light microscope (Olympus BX61VS).

Cellular uptake

Human mammary adenocarcinoma cells, MDA-MB-231, were used to perform the uptake assay. Cells were cultured in DMEM (Sigma-Aldrich) complemented with 10% FBS (Sigma-Aldrich), 2 mM L-glutamine, and 100 U penicillin/0.1 mg/ml streptomycin, and maintained at 37°C in 5% CO_2. Cells were seeded at a density of 15000 cells/cm^2 in 24-well plates, incubated with the different compounds, and the uptake efficiency was observed at 6, 24 and 48 h. CNC-SO_3^- and CNC-ALN were incubated at 70 µg/ml of CNCs. In additional experiments, CNC-DOX and free DOX were used at 0.5 µM of DOX. After incubation, cells were washed and fixed with 4% paraformaldehyde (Bio-Optica) for 45 min. The nuclei were stained with Hoechst-33258 (2 µg/ml in PBS) for 10 min. Cells were analyzed with Olympus Fluoview microscope BX61 with confocal

system FV500 (λ_{exc} 405 nm for Hoechst-33258; λ_{exc} 532 nm to visualize DOX; λ_{exc} 635 nm to visualize Alexa Fluor 633-labelled CNCs). Image quantification was made through Image J software and for each experimental group 10 acquisitions were captured with 20x objective. The values express the ratio between the signal associated with CNCs (area) and the cell number for each field of view.

Cellular viability

Murine macrophage cell line, RAW 264.7, human pre-osteoclasts (OC) derived from peripheral blood mononuclear cells (PBMC) and MDA-MB-231 were employed to assess cellular viability. To obtain OC, PBMC were isolated from three human buffy coats obtained from the blood bank, by gradient centrifugation (Ficoll-Hypaque, GE Healthcare) at 900 g for 30 min, as described elsewhere [18]. Then, PBMC were pooled and washed twice with PBS centrifuging at 760 g for 10 min. PBMC were seeded in 96-well plates in α-MEM containing 20% FBS, 25 ng/ml M-CSF and 50 ng/ml RANK-L (Life Technologies) to be differentiated towards OC. The non-adherent cells were removed three days later by medium renewal. Then, the medium was refreshed every 72 h for 7 days. For both RAW 264.7 and MDA-MB-231, DMEM was used and cells were seeded in 96-well plates. RAW 264.7 and pre-OC were treated with CNC-SO_3^-, CNC-ALN, and free ALN at four doses of ALN (10^{-4}; 10^{-6}; 10^{-8}; 10^{-10} M) for 48 h. MDA-MB-231 cells were treated with CNC-DOX and free DOX at two doses (0.5 and 2 μM) for 6, 24, and 48 h. Cell viability was evaluated by CellTiter 96® AQueous One Solution Cell Proliferation Assay kit (Promega), read in absorbance at 490 nm. Data are presented as proportional viability (%) by comparing the treated group with the untreated cells, the viability of which is assumed to be 100%.

Data Calculation and Statistical Analysis

All data are expressed as mean ± standard error (SEM). Two-way analysis of variance (ANOVA), followed by Sidak's post-test analysis, was used. All statistical analyses were done using the GraphPad Prism version 6.00 for Windows (Graph-Pad Software, San Diego, CA).

Results

Design Synthesis and Characterization of Fluorescently Labelled CNCs

Due to the insertion of half sulfate esters on the CNC surface during the extraction procedure, these samples were named CNC-SO_3^-. The half sulfate esters improved the colloidal stability by a ζ-pot equal to -33.0mV and their amount was determined by conductometric titration and found to be 0.17 mmol/g, confirming our previous study [19]. Then, the primary hydroxyl groups on the nanocrystal surfaces were modified in carboxylic acids through an oxidation reaction mediated by TEMPO, obtaining CNC-COOH. Finally, the nanocrystal surface was further modified with sodium alendronate exploiting the carboxylic groups by EDC coupling with the free amine group of the drug itself (CNC-ALN). To follow the fate of the CNCs *in vitro* and *in vivo* and to assess their biodistribution, a fluorescent tag (Alexa Fluor 633 hydrazide) was attached to the reducing end of CNCs. It was already demonstrated that the Alexa labelling did not modify the CNCs superficial properties [7]. The amount of Alexa bonded to different preparations was kept constant and confirmed by UV-Vis spectroscopy [7]. Figure 1A summarizes the main steps of the synthesis of CNC-ALN.

CNC characterization

Before biological studies, both CNC-SO_3^- and CNC-ALN were characterized to measure the concentration of CNCs in solution (%, w/V) and to assess their main physicochemical parameters, such as size, polydispersity index and surface charge by DLS (Figure 1B). It is noteworthy that the CNC-ALN synthetic procedure led to little, but well detectable modifications of these parameters. However, these changes were somehow expected in case of multi-step processes.

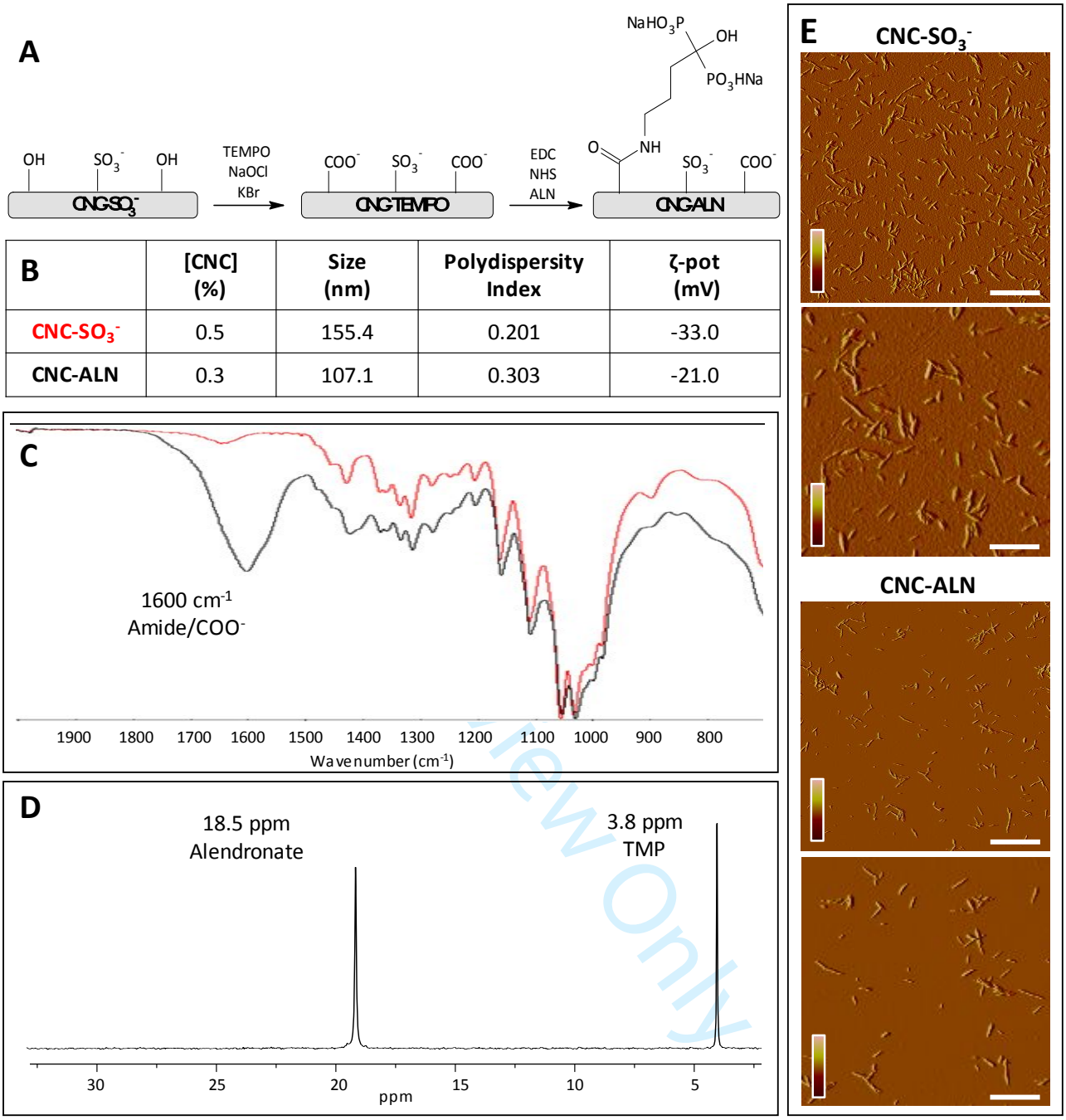

Figure 1: A) Schematic reaction summarizing the multi-step synthesis of the conjugate Cellulose Nanocrystals (CNC-SO_3^-) with Alendronate (CNC-ALN); B) Table summarizing the main physicochemical properties of CNCs determined by DLS; C) FT-IR spectra of CNC-SO_3^- (red) and CNC-ALN (black); D) Representative ^{31}P-NMR spectrum of CNC-ALN. E) Representative tapping mode of AFM images as determined by amplitude error data of CNC-SO_3^- and CNC-ALN after incubation in distilled water. Two different magnifications were reported (for both formulations, upper panels: scale bar 2 µm; lower panels: scale bar 1 µm). Scale color amplitude error: 100/-60 mV.

To qualitatively follow the modification reactions, FT-IR analyses were performed on CNC-SO_3^- and CNC-ALN, as reported in Figure 1C. From the spectra, it was possible to highlight a new band at around 1600 cm^{-1} related to the carboxylate group generated by TEMPO oxidation and its

conversion in amide bond by the EDC coupling with ALN (the two bands are partially overlaid). Another diagnostic modification was the disappearance of the small band at around 900 cm^{-1} related to the primary alcoholic group in C6 position of the anhydroglucan unit, likely due to the selective oxidation promoted by TEMPO. To quantitatively determine the efficacy of the ALN conjugation to CNCs in terms of mmol drug/g of CNCs, ^{31}P-NMR analyses were carried out. Figure 1D reports the spectrum of the synthesized CNC-ALN. Two peculiar peaks were detected: the first at 18.5 ppm refers to the sodium alendronate, the second at 3.8 ppm corresponds to the inner control, the trimethylphosphate (TMP). A spectrum of free ALN was performed as control (data not reported). A peak at 18.5 ppm with a typical chemical shift of the bisphosphonates was detected. In the CNC-ALN spectrum, the first peak evidenced that ALN was actually linked to CNCs and, based on the TMP intensity, that its concentration was 0.77 mmol/g of CNCs (with a loading efficiency of 17%). Finally, to visualize the newly synthesized CNCs, AFM experiments were performed. Figure 1E shows representative images of both CNC-SO_3^- and CNC-ALN at two different magnifications. A rod-like shape was seen for both formulations. In addition, CNCs were monodispersed and similar in size: 7-10 nm thickness and 5-20 nm height. Moreover, two main particle length distributions were observed: 100-150 nm (60%) and 200-350 nm (40%).

CNC-DOX characterization

The amount of DOX (expressed in mg/g of CNCs) bound to the NPs increased as the CNC/DOX ratio (expressed by w/w) decreased, as shown in Figure 2A. Specifically, the data varied from 20 mg/g at 10:1 ratio to 80 mg/g of DOX per g of CNC at 2:1 ratio. The binding efficiency (BE) was roughly 15-20%. Figure 2B shows the cumulative DOX release for CNC-SO_3^- bounded with DOX at different ratios at pH 5.1. In this condition, the % drug released increased with the DOX bounded. According to previous studies, the desorption mechanism was related to the higher solubility of DOX at acidic condition [20]. The maximum release was found in 2:1 loading reaching 80% of DOX at 48 h.

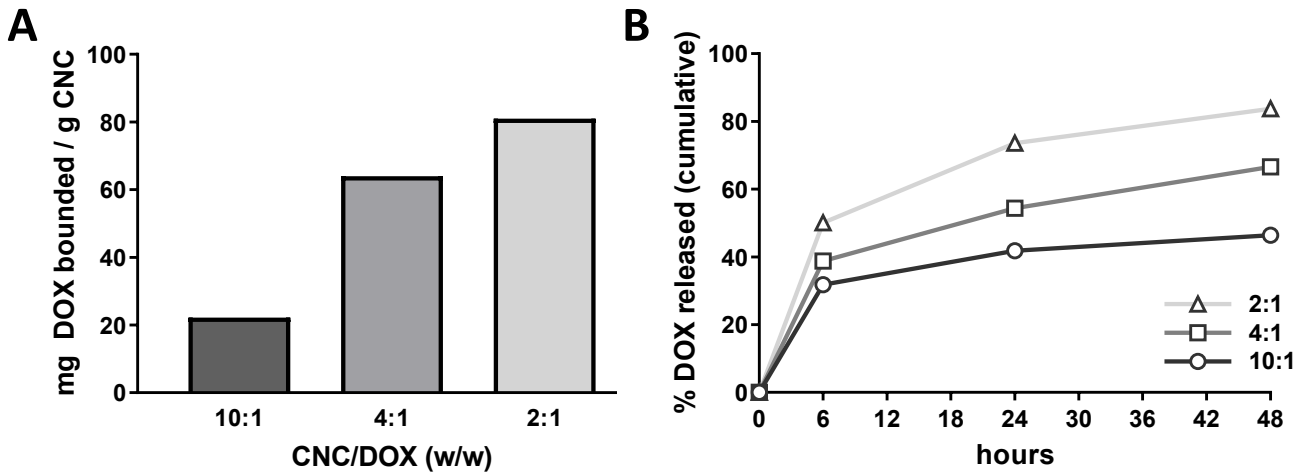

Figure 2: A) DOX loadings (expressed in mg of DOX bounded to 1 g of CNC specimen) to CNC-SO_3^- depending on the CNC/DOX ratio; B) cumulative DOX release in % at pH 5.1 for the CNC-SO_3^- preparation at different loading.

CNC biodistribution

The biodistribution of fluorescently labelled CNC-SO_3^- and CNC-ALN was analyzed in healthy mice by optical imaging technique. Representative whole-body images of vehicle and CNC-treated mice at 4 h are shown in Figure 3A. Mice treated with CNC-SO_3^- confirmed an intense fluorescence diffused in abdominal and thoracic regions. Moreover, a well detectable signal was observed in hind legs. A higher magnified picture (bottom panel) confirmed the presence of signal along bones and joints. CNC-ALN showed a similar pattern of fluorescence and maintained a peculiar tropism toward hind legs. In both experimental groups, a progressive reduction of the signal was detected until 96 h, without difference in their kinetics (data not shown). To better evaluate the tropism of CNCs to the skeletal system, an *ex vivo* study was carried out by scanning isolated bones at selected time points. Figure 3B shows vertebral columns, femurs, tibias and distal hind legs of animals sacrificed 4 h after the administration of the vehicle, CNC-SO_3^- or CNC-ALN. A strong and homogeneous signal was observed in bones in both CNC groups, with the highest intensity in the vertebral columns and distal hind legs. The longitudinal quantification of the signal in bones of treated animals is shown in Figure 3C. Vertebral columns and distal hind legs had a higher level of signal compared to the femurs and tibias. In the vertebral column, a high level of signal was observed 4 h after administration with a drastic reduction within the first 24 h in both groups. In

distal hind legs, the trend of the fluorescence was similar to that measured in vertebral columns. CNC-ALN treated mice showed a milder reduction of fluorescence at two later time points.

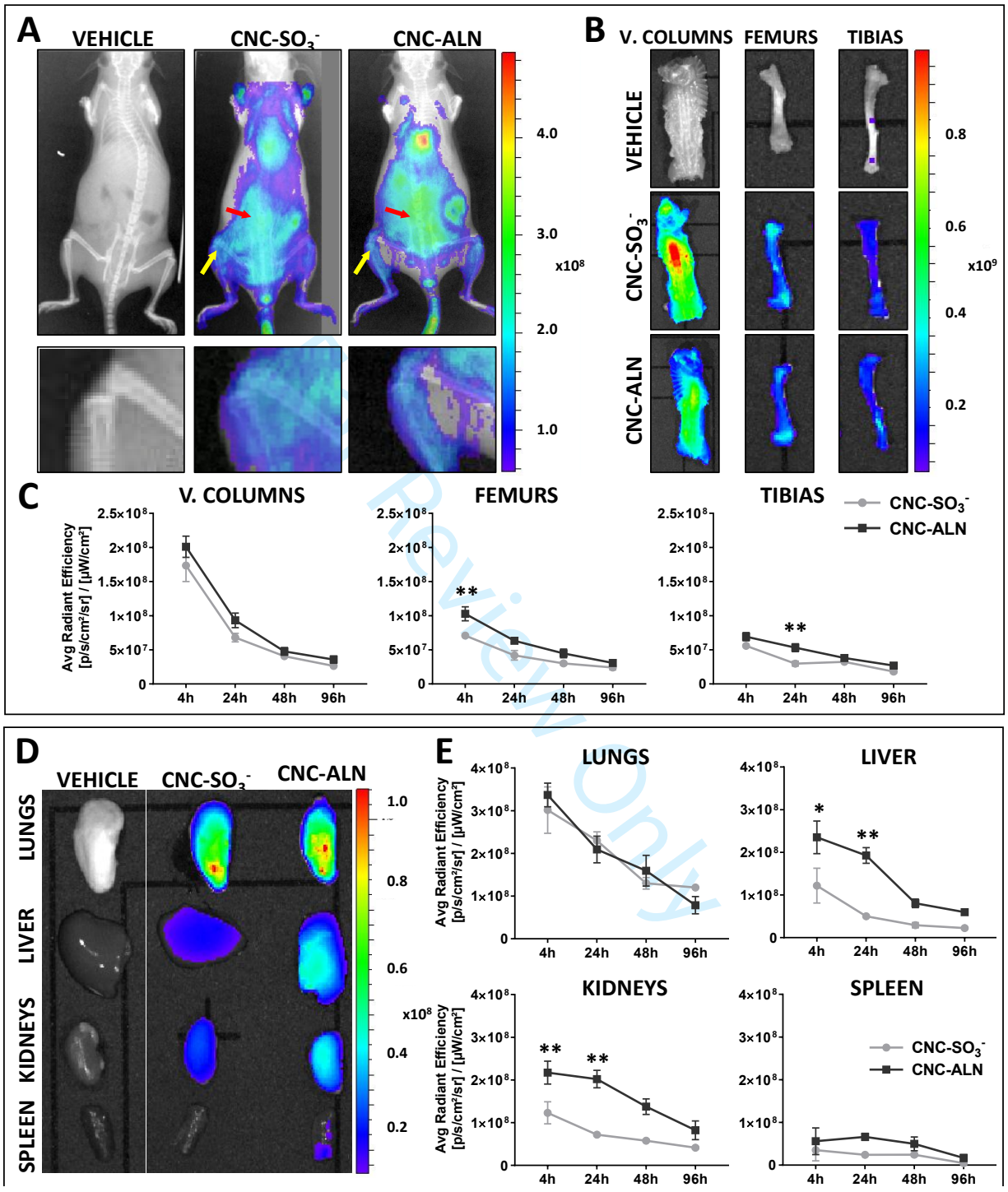

Figure 3: A) *In vivo* optical and X-rays imaging of the vehicle-, CNC-SO_3^-- and CNC-ALN-treated mice 4 h after IV administration. In upper panels, representative total body scans are reported. In the lower panels, higher magnified images of the knee joint are depicted. B) Representative pictures of the vertebral columns, femurs, and tibias of mice treated with vehicle, CNC-SO_3^- or CNC-ALN 4 h after treatment. C) Diagrams showing the trend of signal intensity in bones of mice treated with CNC-SO_3^- or CNC-ALN. **D**) *Ex vivo* optical imaging of lungs, liver, kidneys and spleen from vehicle-, CNC-SO_3^-- and CNC-ALN-treated animals sacrificed 4 h after IV administration. E) Diagrams showing the trend of signal intensity in organs from animals treated with CNC-SO_3^- and CNC-ALN. A, B, D) The fluorescence signal intensity, measured as radiant efficiency, is shown as a pseudo-color scale bar. The

pseudo-color scale bar is consistent for all images to show relative changes of biodistribution over time. C, E) All data are expressed as mean ± SEM and analyzed by Two-way ANOVA followed by Sidak Post-hoc test. *<0.05, **<0.005 CNC-SO_3^- vs. CNC-ALN. The overall influence of time for all the bones, lungs, livers and kidneys is p<0.0001.

Ex vivo imaging of lungs, liver, kidneys, and spleen of mice sacrificed 4 h after injection of vehicle, CNC-SO_3^- or CNC-ALN is shown in Figure 3D. Both CNCs had a high tropism toward the lungs and showed low accumulation in the spleen. Interestingly, a low accumulation of CNC-SO_3^- was found in the kidneys and liver, while the functionalization with ALN led to an increased CNCs accumulation at 4 and 24 h after injection in these organs. Over time an almost linear decay of the signal was observed in all organs of both CNC-SO_3^- or CNC-ALN-treated mice, although the signal was still detectable 96 h after treatment (Figure 3E).

To better characterize the localization of CNCs, confocal microscopy of liver, kidneys, and lung section was carried out in mice sacrificed 4 or 96 h after administration (Figure 4). In the liver sections of CNC-ALN-treated mice, the fluorescent signal was detected at both time points (4 and 96 h) multifocally at the level of cells localized in the parenchyma along the sinusoids. Differently, in CNC-SO_3^--treated mice the signal was localized at the blood vessel walls only at 4 h after treatment, and no signal was observed in the parenchyma at both time points. A marked accumulation of CNCs in blood vessel walls was observed in the kidneys of mice treated with CNC-SO_3^- and CNC-ALN at both time points. No accumulation was observed in the other renal structures. In the lungs, an intense and protracted fluorescence signal was detected in both the experimental groups with similar distribution and intensity until 96 h. The signal appeared as continuously distributed along the alveolar structures and was detected also at blood vessel walls and at the periphery of the bronchioles.

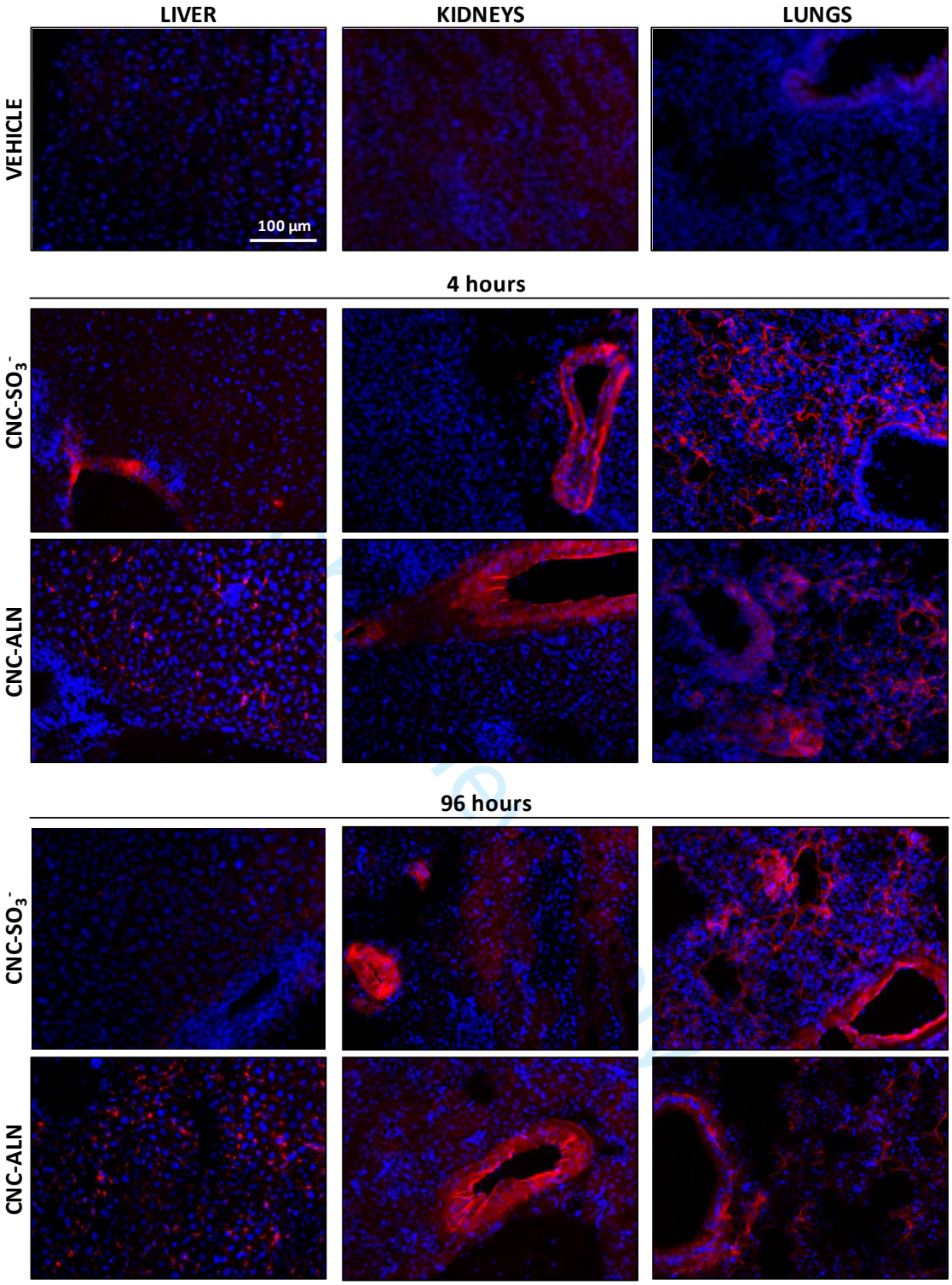

Figure 4: Representative pictures showing the tissue distribution of CNC-SO_3^- or CNC-ALN (red signal) in liver, kidneys, and lung 4 and 96 h after treatment. In the upper panel, the sections were excited with the laser associated with the excitation peak of CNCs, but as expected, no signal was revealed. Hoechst-33258 staining (blue dots) has been used to stain the nuclei.

No treatment-related histopathological changes were observed at 96 h in the lungs of both CNC-SO_3^- and CNC-ALN-treated mice (Figure 5).

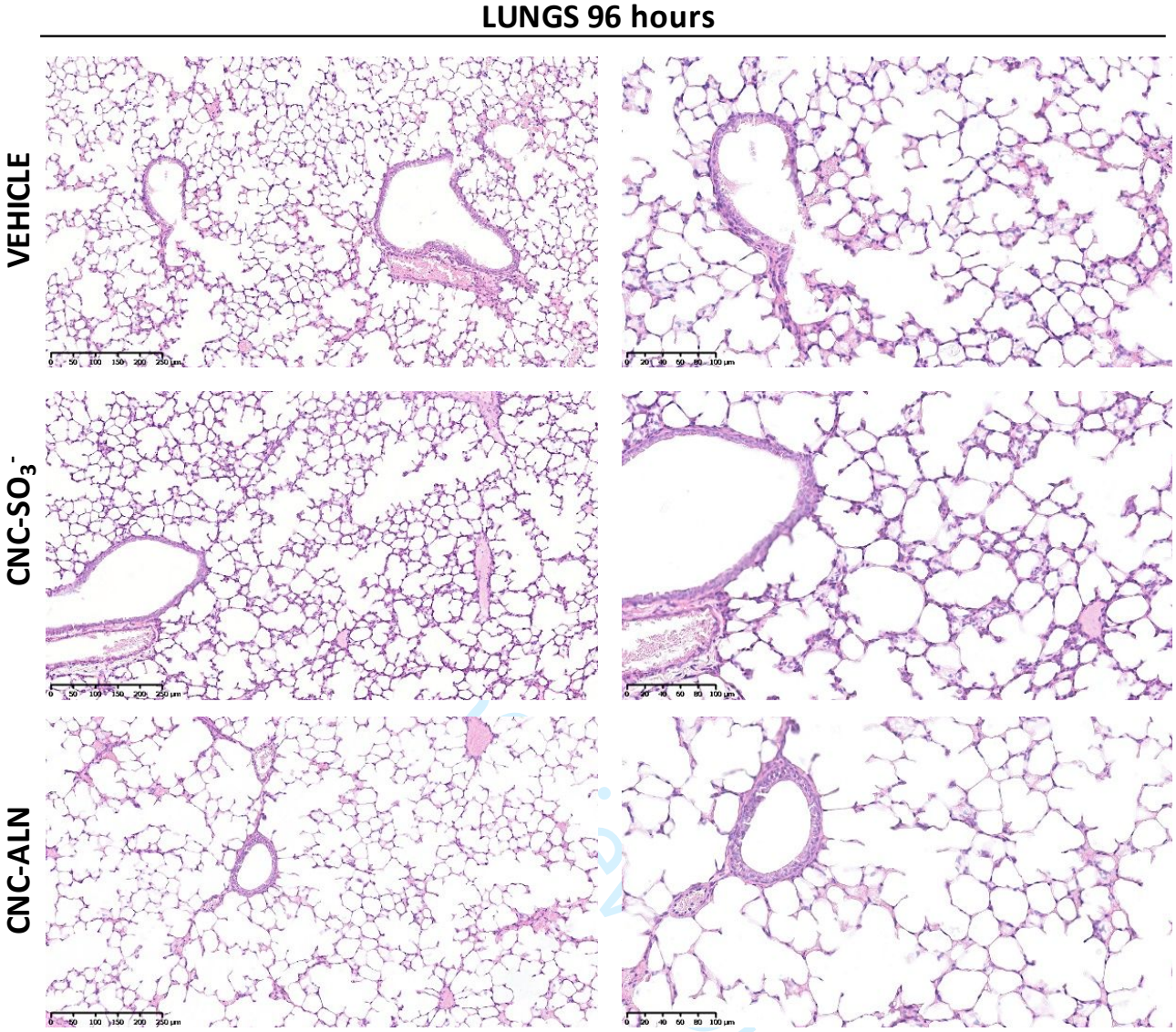

Figure 5: Histological evaluation by Haematoxylin and Eosin staining of lung tissues of mice treated with vehicle, CNC-SO_3^- and CNC-ALN and sacrificed 96 h after the treatment.

Cell target interaction

Figure 6A shows the process of internalization of both CNC-SO_3^- and CNC-ALN in MDA-MB-231 after 24 h of incubation. Lower magnification images revealed an almost heterogeneous penetration of CNCs. As expected, CNC-SO_3^- exclusively localized in the cytoplasm, with the spotty staining suggesting their clusterization in vesicles. No relevant change of intracellular localization was observed when cells were incubated with CNC-ALN. On the contrary, the uptake efficiency (expressed as the ratio between the red signal area and nuclei, normalized to the single-cell) was higher in CNC-ALN-treated cells (Figure 6B).

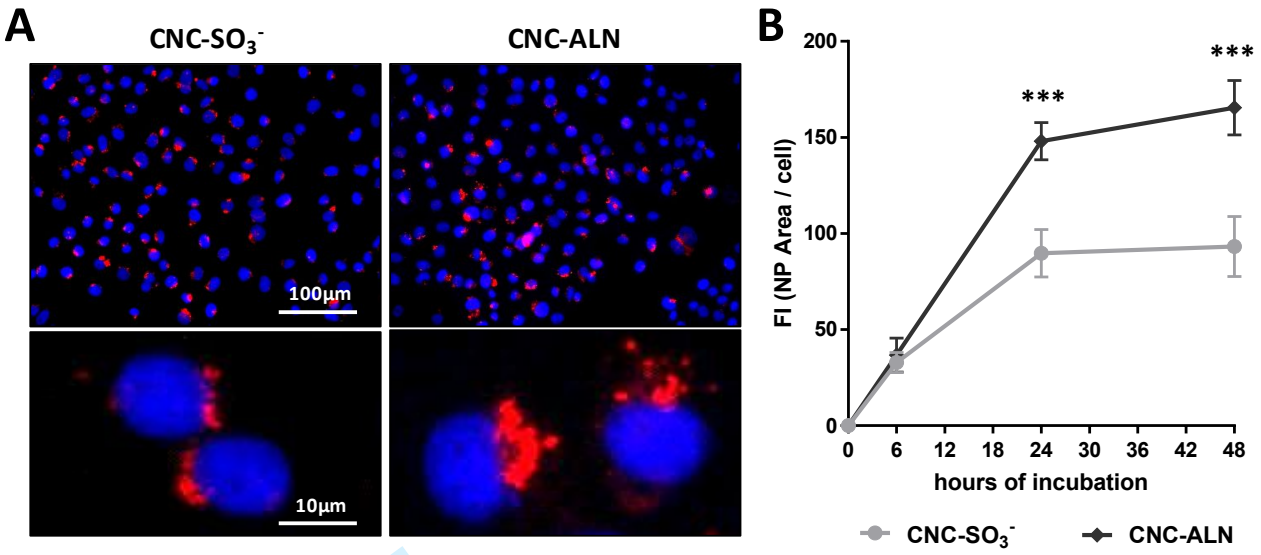

Figure 6: A) Representative images showing the presence of both CNC-SO_3^- and CNC-ALN in MDA-MB-231 cells 24 h after incubation. In the upper panel, a field of view with a quite large number of cells and a single cell staining are depicted in the upper and lower panel, respectively. CNCs are visualized in red (Cy5 signal) and nuclei in blue (Hoechst-33258 staining). B) Quantification of cellular uptake 6, 24 and 48 h after treatment. The data are expressed as mean ± SEM and analyzed by Two-way ANOVA followed by Sidak Post-hoc test. ***<0.0005 CNC-SO_3^- vs. CNC-ALN. The overall influence of time is p<0.0001.

After evaluating the internalization efficiency of both CNC-SO_3^- and CNC-ALN, the loading of ALN into CNCs was analyzed to assess a potential decrease of its therapeutic activity. To do this, the effect of free ALN or ALN linked to CNCs, was evaluated in both RAW 264.7 and pre-OC at different doses after 48 h of incubation (Figure 7).

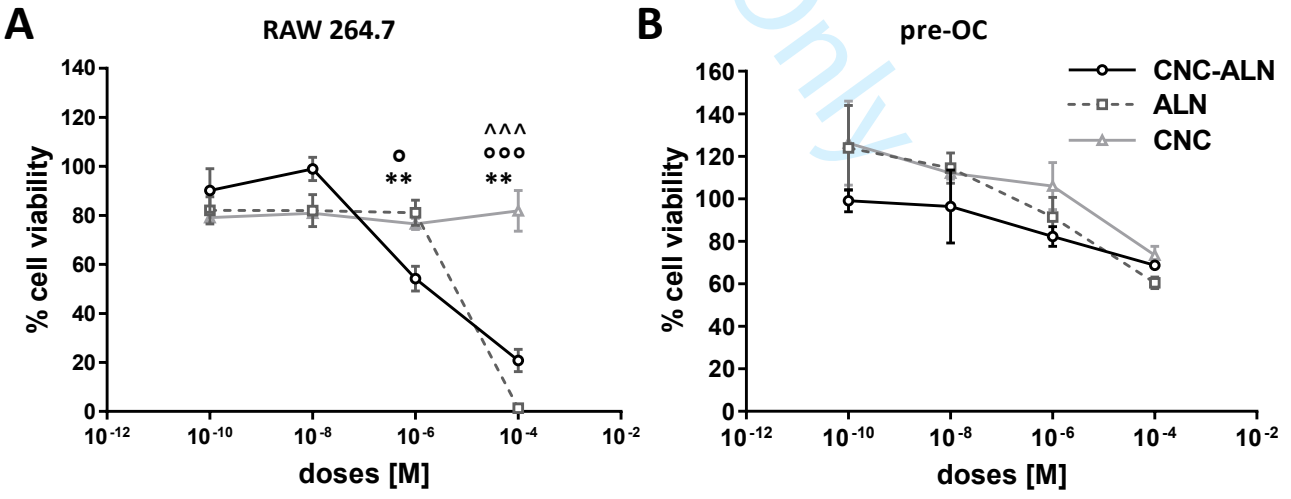

Figure 7: MTS assay performed incubating A) RAW 264.7 and B) pre-OC with ALN free or linked to CNCs at the following concentrations (10^{-10}, 10^{-8}, 10^{-6}, 10^{-4} M) for 48 h of incubation. The same amount of CNC linked to ALN was incubated without the drug to evaluate the effect of CNC alone. Data are expressed as mean ± SEM and analyzed by Two-way ANOVA followed by Sidak Post-hoc test. *<0.05, **<0.005, ***<0.0005. *ALN vs. CNC-ALN, °CNC vs. CNC-ALN, ^CNC vs. ALN.

Figure 7A clearly shows that both free ALN and CNC-ALN were able to reduce macrophage viability at higher doses than 10^{-6} M. Not surprisingly, CNCs alone did not affect cell viability. As shown in Figure 7B, a dose-dependent trend was observed in pre-OC. At lower doses (10^{-10} and 10^{-8} M), CNC-ALN yielded lower cell viability compared to CNCs and free ALN, although these differences were not statistically significant. At higher doses, CNC-ALN and ALN showed comparable effects. The cytotoxic effect of CNCs alone increased at the highest concentration.

Finally, the effect of CNCs linked to anticancer agents (DOX) was tested in MDA-MB-231 cells. Figure 8A shows the cellular uptake of free DOX or DOX linked to CNCs also exploiting the fluorescence of the drug ($\lambda_{emission}$ 591 nm). Data demonstrated that free DOX localized into the nucleus, the target subcellular organelle of the drug. Notably, the violet signal in the higher magnified picture clearly demonstrated the co-localization with the nucleus. On the other hand, only a mild release of DOX from CNCs was detectable at this time point. In fact, the spotted red fluorescent signal showed some molecules of DOX still attached to CNCs, confined and clustered into endocytic vesicles. The diagram in Figure 8B shows that: i) a time-dependent effect was observed independently of the type of formulation; ii) in both formulation the DOX concentration played a role in reducing the overall survival 24 h and 48 h after treatment; iii) the effect of concentration was markedly higher for the nanoformulation compared to DOX alone.

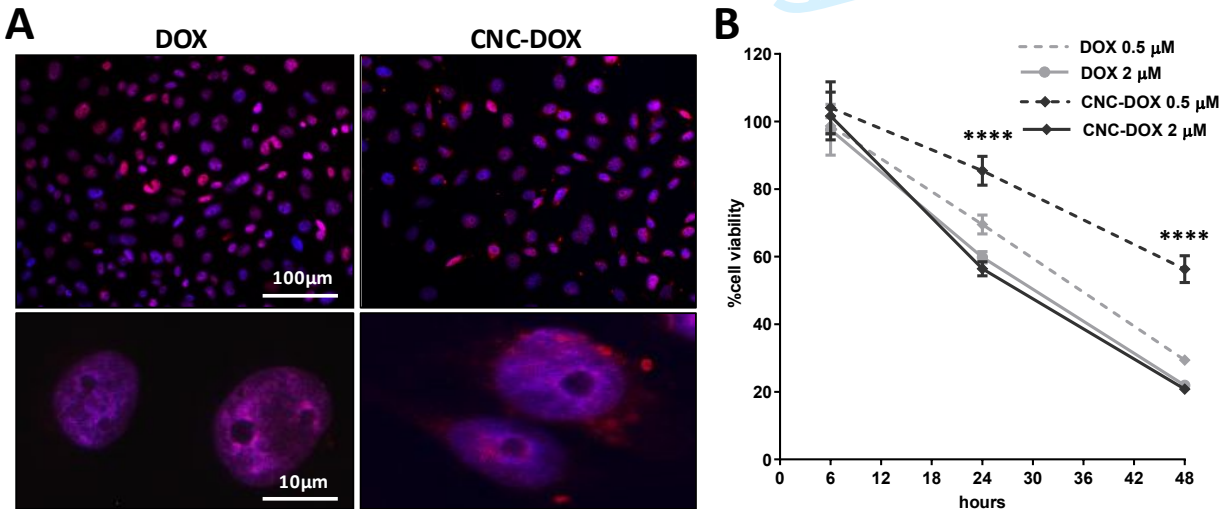

Figure 8: A) Representative confocal microscopy images showing internalization of 0.5 µM of DOX free or conjugated to CNCs (red signal represents DOX autofluorescence) in MDA-MB-231 cells after 24 h of incubation. Two levels of magnification were

reported. Nuclei are visualized in blue (Hoechst-33258 staining) and DOX in red. B) Diagram showing the toxicity of DOX free or conjugated to CNCs in MDA-MB-231 cells, at two different doses (0.5 and 2 μM). Data are represented as mean ± SEM and analyzed by Two-way ANOVA followed by Sidak Post-hoc test. ****<0.0001 DOX vs. CNC-DOX at 0.5 μM. No significant difference was found comparing DOX vs. CNC-DOX at 2 μM. The overall influence of time is p<0.0001.

Discussion

Osteoporosis and breast cancer-derived bone metastases are increasing in incidence, morbidity and mortality in women [21,22]. In spite of the *in vitro* evidence of specific pharmacological tools for both therapies, there are several hurdles that dramatically reduce their efficacy in patients. They mainly include low stability, short plasmatic half-life, poor bioavailability in bones and hazardous accumulation in off-target organs [10–13,23].

The present study was therefore aimed at developing delivery systems to improve the targeting of either anti-cancer or anti-osteoporosis drugs, in the attempt to somehow overcome the aforementioned pharmacokinetic limitations. To this aim, we synthesized innovative nanocarriers based on CNC backbone. Our *in vivo* results confirmed that the peculiar physicochemical properties of CNCs greatly increased the ratio of bone/filter organs. Indeed, CNCs due to their elongated shape and thin size establish direct contact with the vessel walls and escape from the bone microvasculature, which favors the interaction with the cationic surface of the bone matrix, by their negative charges [3,7,24]. The reliability of our tracking derived from our ability to covalently link both ALN and the fluorescent dye to CNCs. This strongly reduced the risks of biological elution of the cargo and the dye after intravenous administration and/or incubation in medium [25].

Our experimental evidence demonstrated that a specific tropism among the different bones occurred. The main tropism was detected in the vertebral column and the femoral epiphysis. This suggested a different uptake between cancellous and cortical bone. In particular, the greater uptake of cancellous bone could be related to the bone turnover and blood flow, rather than to the bone density. Moreover, ALN linkage did not modify this peculiar interaction, as a significant increase of signal was seen in femurs (4 h) and in tibias (24 h) of CNC-ALN compared to CNC-SO^{3-} treated

mice. No difference in the overall trend was observed. However, there was a significant time-dependent reduction. We also demonstrated that the presence of ALN did not induce any perturbation to CNC peculiar tropism. Similarly to other negatively charged nanotubes and nanorods, CNCs poorly accumulated in the liver and spleen [3,26]. However, a significant increase of uptake from resident liver macrophages was found in animals treated with CNC-ALN compared to those receiving CNC-SO_3^-. Although such behavior could be ascribed to several factors, further *in vitro* experiments, showing the same difference among CNC-ALN and CNC-SO_3^- in terms of internalization in RAW 264.7, led us to hypothesize that the higher stealthiness of CNC-SO_3^- can be due to a lower bioavailability. Our characterization revealed that, during the process of CNC-ALN formation, there was a significant shortening of the nanocrystal. It is therefore possible to argue that, as previously reported, a margination of nanoparticles in capillaries as a function of their size and shape can occur [27]. It was quite reasonable that intravenously injected extremely thin and negatively charged nanoparticles could rapidly interact with the renal tubular system; also in this case CNC-ALN seemed to better interact with the organ parenchyma. Overall, the nanoparticle accumulation in the lungs, in this case without any difference between the two treatments, is associated with a very large size or the occurrence of aggregations. However, fluorescent images highlighted the presence of stretched structures, mainly associated with endothelial cells. This tropism could be of interest for the development of other targeted systems against pulmonary disorders. However, to this aim, although no evidence of relevant histological alterations was observed in mice sacrificed 4 days after the treatment, a deeper investigation after a repeated treatment should be carried out.

One of the main hurdles in the clinical management of patients assuming bisphosphonates is the poor oral absorption. Therefore, the parenteral administration has been taken into consideration in recent years. Bisphosphonate pharmacokinetics shows a rapid and homogenous distribution in bone and soft organs, in particular kidneys and spleen, but they are also rapidly cleared by renal filtration with a plasmatic half-life of 90 min [28,29].

Our data showed that the linkage with CNC enables us to maintain ALN in different organs, including bones for a long time. In terms of efficacy, the combination of CNCs and ALN seemed to slightly increase the cytotoxic effect of ALN on osteoclast precursors, at least at lower doses. The lack of a clear effect of both ALN and CNC-ALN on pre-OC may depend on the short pre-differentiation period chosen to induce primary PBMC into OC. Additionally, cytotoxicity might not be the primary mechanism of action of ALN, which could exert a more relevant action on osteoclast differentiation [30].

Another important aim of this study was the adsorption of the anticancer agent DOX into CNCs. It has been already demonstrated that the administration of DOX by liposomes dramatically reduces the side effects and the off-targeting [31]. However, this strategy does not improve the ability to reach the bone target. In this context, we found that the use of charged particles (negatively for CNCs) to bind and release basic drugs (such as DOX) is well established [32]. To avoid modifications of the CNC surface and maintain a good colloidal suspension stability and bone targeting, a strategy based on surface adsorption has been undertaken [17,32]. The CNC-DOX preparations were not characterized in term of physicochemical properties, anyways only a limited decreasing of colloidal stability was observed (directly related to the DOX bounded) in agreement with a reported decreasing of ζ-potential [17,20]. The mechanism of adsorption was based on hydrophobic, hydrogen-bond and electrostatic interactions [20,33]. It is important to underline that, in contrast to previous studies, we found a lower binding efficacy [17]. However, this reduction was counterbalanced by a better purity of our nanocarrier through the deeper washing procedure adopted. The observed difference seemed to play an important role also during drug release investigations, where CNCs showed a faster but more controlled release than that reported in the literature [17]. Notably, the presence of the CNC backbone did not modify the well-established effect of DOX, even if a slight decrease of the cytotoxicity was observed due to the slow penetration of the drug when incubated as nanoformulation. It is well known that the interest of nanoparticles in medicine has emerged from their ability to reduce the side effects and therefore to

increase the therapeutic index of DOX [31]. In this context, the efficacy of CNC-DOX against breast cancer cells and the overall ability of CNCs to bind bones represent an added value to improve the pharmacotherapy in breast-derived bone metastases.

Conclusions

The main innovative hallmark of nanomedicine is the possibility to improve organ specificity of an extended range of drugs, therefore reducing side effects and risks [34]. Nanocellulose possesses diverse characteristics different from traditional materials, including peculiar size and shape, crystallinity, high specific surface area, surface chemical reactivity, biocompatibility, lack of toxicity and relatively low cost, making it an interesting nanomaterial for biomedical applications [35,36]. The functionalization reactions can also be extended to other chemical compounds, as for ALN and DOX, for future development of CNCs as therapeutic agents in severe bone-related diseases, in addition to osteoporosis and bone metastases.

Summary point.

- Alendronate (ALN) and Doxorubicin (DOX) were conjugated to CNC backbone to reduce their off-target organ accumulation and to improve their therapeutic efficacy.
- Chemical coupling of ALN and CNC was achieved through an amide bond exploiting an oxidation reaction. The loading of DOX was achieved through direct adsorption of the drug on CNC-SO_3^-.
- *In vivo* and *ex vivo* imaging studies demonstrated a specific tropism of CNC nanoformulations among the different bones for a long time.
- ALN linkage did not modify the CNC behavior, nevertheless the liver and kidney accumulation resulted slightly higher than CNC alone.
- CNC-ALN shows a dose and time-dependent trend on macrophage and pre-osteoclast viability.

- CNC-DOX did not modify the cytotoxic effect of DOX, even if at low dose the nanoformulation decreased DOX activity due to the slow penetration of the drug.

References

Papers of special note have been highlighted as: • of interest; •• of considerable interest.

1. Ventola CL. Progress in nanomedicine: approved and investigational nanodrugs. *P T*. 42(12), 742–755 (2017).

2. Farokhzad OC, Langer R. Impact of nanotechnology on drug delivery. *ACS Nano*. 3(1), 16–20 (2009).

3. Blanco E, Shen H, Ferrari M. Principles of nanoparticle design for overcoming biological barriers to drug delivery. *Nat Biotechnol*. 33(9), 941–951 (2015). •

• This study clearly demonstrates that nanoparticle size, shape and surface charge dictate the biodistribution.

4. Faria M, Björnmalm M, Thurecht KJ, *et al.* Minimum information reporting in bio–nano experimental literature. *Nat Nanotechnol*. 13(9), 777–785 (2018). •

• This study presents a "minimum reporting standard" for studies investigating bio-nano interactions.

5. Hirabayashi H, Fujisaki J. Bone-specific drug delivery systems: approaches via chemical modification of bone-seeking agents. *Clin Pharmacokinet*. 42(15), 1319–1330 (2003).

6. Habibi Y, Lucia LA, Rojas OJ. Cellulose nanocrystals: chemistry, self-assembly, and applications. *Chem Rev*. 110(6), 3479–3500 (2010).

7. Colombo L, Zoia L, Violatto MB, *et al.* Organ distribution and bone tropism of cellulose nanocrystals in living mice. *Biomacromolecules*. 16(9), 2862–2871 (2015). ••

•• This study proves the ability of cellulose nanocrystals to interact with bones, exploiting the chemical interaction between the $Ca^{(2+)}$ of the bone matrix and the active surface of negatively-charged nanocrystals.

8. Poole KE, Compston JE. Bisphosphonates in the treatment of osteoporosis. *BMJ*. 344, e3211 (2012).

9. Sledge GW, Neuberg D, Bernardo P, *et al.* Phase III trial of doxorubicin, paclitaxel, and the combination of doxorubicin and paclitaxel as front-line chemotherapy for metastatic breast cancer: an intergroup trial (E1193). *J Clin Oncol*. 21(4), 588–592 (2003).

10. Perazella MA, Markowitz GS. Bisphosphonate nephrotoxicity. *Kidney Int.* 74(11), 1385–1393 (2008).

11. Kennel KA, Drake MT. Adverse effects of bisphosphonates: implications for osteoporosis management. *Mayo Clin Proc.* 84(7), 632–637; quiz 638 (2009).

12. Swain SM, Whaley FS, Ewer MS. Congestive heart failure in patients treated with doxorubicin: a retrospective analysis of three trials. *Cancer*. 97(11), 2869–2879 (2003).

13. Singal PK, Iliskovic N. Doxorubicin-induced cardiomyopathy. *N Engl J Med.* 339(13), 900–905 (1998).

14. Barana D, Salanti A, Orlandi M, Ali DS, Zoia L. Biorefinery process for the simultaneous recovery of lignin, hemicelluloses, cellulose nanocrystals and silica from rice husk and Arundo donax. *Ind Crops Prod*. 86, 31–39 (2016).

15. Saito T, Isogai A. Tempo-mediated oxidation of native cellulose. The effect of oxidation conditions on chemical and crystal structures of the water-insoluble fractions. *Biomacromolecules*. 5(5), 1983–1989 (2004). •

• This study explains the procedure to functionalize cellulose nanocrystals, through TEMPO-mediated oxidation

16. Huang C-F, Chen J-K, Tsai T-Y, Hsieh Y-A, Andrew Lin K-Y. Dual-functionalized cellulose nanofibrils prepared through TEMPO-mediated oxidation and surface-initiated ATRP. *Polymer*. 72, 395–405 (2015). ••

•• This study explains the procedure to functionalize cellulose nanocrystals, through TEMPO-mediated oxidation

17. Letchford, Jackson, Wasserman B, Ye, Hamad W, Burt H. The use of nanocrystalline cellulose for the binding and controlled release of drugs. *Int J Nanomedicine*. 6, 321-330 (2011).

18. Bongio M, Lopa S, Gilardi M, Bersini S, Moretti M. A 3D vascularized bone remodeling model combining osteoblasts and osteoclasts in a CaP nanoparticle-enriched matrix. *Nanomedicine*. 11(9), 1073–1091 (2016).

19. D'Orazio G, Munizza L, Zampolli J, *et al.* Cellulose nanocrystals are effective in inhibiting host cell bacterial adhesion. *J Mater Chem B*. 5(34), 7018–7020 (2017).

20. Akhlaghi SP, Tiong D, Berry RM, Tam KC. Comparative release studies of two cationic model drugs from different cellulose nanocrystal derivatives. *Eur J Pharm Biopharm*. 88(1), 207–215 (2014). ••

•• This study shows the desorption mechanism to load cellulose nanocrystal with model drug compounds.

21. Black DM, Rosen CJ. Postmenopausal osteoporosis. *N Engl J Med*. 374(21), 2096–2097 (2016).

22. Coleman RE. Clinical features of metastatic bone disease and risk of skeletal morbidity. *Clin Cancer Res.* 12, 6243s–6249s (2006).

23. Cheng H, Chawla A, Yang Y, *et al.* Development of nanomaterials for bone-targeted drug delivery. *Drug Discov Today*. 22(9), 1336–1350 (2017).

24. Soares AP, do Espírito Santo RF, Line SRP, *et al.* Bisphosphonates: pharmacokinetics, bioavailability, mechanisms of action, clinical applications in children, and effects on tooth development. *Environ Toxicol Pharmacol*. 42, 212–217 (2016).

25. Tenuta T, Monopoli MP, Kim J, *et al.* Elution of labile fluorescent dye from nanoparticles during biological use. *PLoS One*. 6(10), e25556 (2011).

26. Talamini L, Violatto MB, Cai Q, *et al.* Influence of size and shape on the anatomical distribution of endotoxin-free gold nanoparticles. *ACS Nano*. 11(6), 5519–5529 (2017).

27. D'Apolito R, Tomaiuolo G, Taraballi F, *et al.* Red blood cells affect the margination of microparticles in synthetic microcapillaries and intravital microcirculation as a function of their size and shape. *J Control Release*. 217, 263–272 (2015). •

• This study explains how it is possible to promote particle contact and adhesion to the vesselwall.

28. Cremers S, Papapoulos S. Pharmacology of bisphosphonates. *Bone*. 49(1), 42–49 (2011).

29. Baroncelli GI, Bertelloni S. The use of bisphosphonates in pediatrics. *Horm Res Paediatr*. 82(5), 290–302 (2014).

30. Lee D, Heo DN, Kim H-J, *et al.* Inhibition of osteoclast differentiation and bone resorption by bisphosphonate-conjugated gold nanoparticles. *Sci Rep*. 6, 27336 (2016).

31. Cagel M, Grotz E, Bernabeu E, Moretton MA, Chiappetta DA. Doxorubicin: nanotechnological overviews from bench to bedside. *Drug Discov Today*. 22(2), 270–281 (2017).

32. Guo X, Chang R-K, Hussain MA. Ion-exchange resins as drug delivery carriers. *J Pharm Sci*. 98(11), 3886–3902 (2009).

33. He X, Male KB, Nesterenko PN, Brabazon D, Paull B, Luong JHT. Adsorption and desorption of methylene blue on porous carbon monoliths and nanocrystalline cellulose. *ACS Appl Mater Interfaces*. 5(17), 8796–8804 (2013).

34. Shi J, Votruba AR, Farokhzad OC, Langer R. Nanotechnology in drug delivery and tissue engineering: from discovery to applications. *Nano Lett.* 10(9), 3223–3230 (2010).

35. Lin N, Dufresne A. Surface chemistry, morphological analysis and properties of cellulose nanocrystals with gradiented sulfation degrees. *Nanoscale*. 6(10), 5384–5393 (2014).

36. Mondal S. Preparation, properties and applications of nanocellulosic materials. *Carbohydr Polym*. 163, 301–316 (2017).

ABSTRACT

Aim: Herein, we investigated the use of Cellulose Nanocrystals (CNCs) as drug nanocarriers combining an anti-osteoporotic agent, alendronate (ALN), and an anti-cancer drug, doxorubicin (DOX). **Materials & methods:** CNC physicochemical characterization, *in vivo* imaging coupled with histology, *in vitro* uptake and toxicity assays were carried out. **Results:** *In vivo* CNC-ALN did not modify bone tropism and lung penetration, whereas its liver and kidneys accumulation resulted slightly higher compared to CNCs alone. *In vitro* studies showed that CNC-ALN did not impair the ALN effect on osteoclasts, while CNC-DOX confirmed the therapeutic potential against bone metastatic cancer cells. **Conclusions:** This study provides robust proofs about the potential of CNCs as easy, flexible and specific carriers to deliver compounds to the bone.

KEYWORDS

Cellulose Nanocrystals, Drug Delivery System, Surface Functionalization, Bone Tropism.

Introduction

One of the main challenges of pharmacological research is to develop or optimize targeted delivery systems to make systemic drug administration safer and more effective. With this aim, in the last two decades, different strategies have been investigated to deliver drugs by linking a targeting or penetrating agent to the therapeutic compound. Many of these systems, such as viral vectors, antibodies, peptides and liposomal formulations are already available for patients, while others are still under preclinical evaluation, including nanocarriers [1]. Nanocarriers have major advantages since they can load a great number of therapeutic agents and modulate their release, increasing the stability and reducing the off-target delivery. Nanocarriers can be "multitasking", enclosing targeting moieties, contrast agents or other compounds able to control the drug release depending on specific environmental conditions (e.g. pH, redox state, ionic composition) [2]. Moreover, slight modifications of physicochemical characteristics of nanoparticles, such as size, shape, surface charge, and coatings, can be exploited to modulate their interaction with the host [3]. In this context, it has been recently claimed that an overall characterization of bio-nano interaction should be carried out in the process of nanoparticle development in biomedicine [4].

Despite several decades of progress~~es~~, bone-specific delivery is still limited by the unique anatomical features of bone. A practical solution is to produce targeted drugs with high affinity for hydroxyapatite [5]. Among the broad range of materials tested in the last decades, Cellulose NanoCrystals (CNCs), obtained from cellulose in a defect-free rod-like crystalline state, have attractive properties including high surface area, low density and good mechanical strength [6]. Our previous data demonstrated that CNCs show a high tropism toward bones, with low accumulation in filter organs and fast excretion, without detrimental effects both *in vivo* and *in vitro* [7]. Starting from these promising results, in the present study, we built-up CNCs linked with two different compounds, sodium alendronate (ALN) or doxorubicin (DOX), known for their efficacy to counteract the osteoporotic bone demineralization and to limit the metastatic spread of breast cancer cells to bone, respectively [8,9]. Despite their proven efficacy, both these drugs cause side effects

due to their off-target organ accumulation [10–13]. To overcome this limitation, we optimized the linkage of ALN to CNCs through an amide bond exploiting the carboxylic acid function introduced to CNC surface through an oxidation reaction. The loading of DOX was instead achieved through direct adsorption on CNC-SO_3^-. These new formulations were extensively characterized in terms of chemistry, morphology and drug release. Since a slight change in the nanocarrier structure can modify its tropism, we compared the biodistribution of CNC-SO_3^- and CNC-ALN after systemic injection in healthy mice. Finally, the ability to penetrate filter (macrophages) and target cells (osteoclasts for ALN and breast cancer cell line for DOX) were assessed.

Materials & Methods

CNC extraction

CNCs were extracted from Whatman#1 filter paper (Sigma-Aldrich) by acid hydrolysis according to a previously reported procedure [14]. In particular, 10 g of filter paper were treated with 64% H_2SO_4 for 1 h at 55°C with an acid/cellulose ratio of 10 w/w. After acidic treatment, the content of the flask was poured into a 10-fold volume of cold water and stirred. Cellulose sediment was purified by repeated centrifugations at 3200 g for 15 min, and the solid component was suspended in distilled water by ultrasonic mixing for 5 min. Then, the suspension was dialyzed against ultrapure Milli-Q water for 1 week until reaching pH 6. CNC-SO_3^- were recovered in about 40% yield, giving 400 ml of suspension at 1% w/V concentration.

CNC-ALN synthesis

The synthesis was accomplished following the procedure already reported in literature. Briefly, CNCs were submitted to a TEMPO (2,2,6,6-tetramethylpiperidine-1-oxyl radical, Sigma-Aldrich) mediated oxidation [15,16]. CNC-TEMPO were obtained at 50% yield, at a final concentration of 0.5% w/V. The synthesis of ALN-conjugated CNCs was carried out to 10 ml of 0.5% w/V CNC-TEMPO suspension (available carboxylic acid content: 0.92 mmol/g, titration). 1-ethyl-3-(3-dimethylaminopropyl) carbodiimide (EDC, 0.23 mmol, 191.7 g/mol) (Fluka Analytical) and N-

hydroxysuccinimide (NHS, 0.23 mmol, 115.1 g/mol) (Sigma Aldrich) were weighed in 5-fold molar excess, dissolved in 1 ml of bidistilled water, then added to the CNC suspension under stirring. After 1 h, a 5-fold molar excess of Sodium Alendronate (0.23 mmol, 325.1 g/mol) (Sigma-Aldrich) was added, the pH adjusted to 6.3-6.5 by adding 0.1 M phosphate buffer saline (Lonza), and the mixture was left to react overnight at RT. Purification of CNC-ALN was achieved through precipitation in EtOH/phosphate buffer solution (4:1), centrifugation (3200 g, 15 min, 2 cycles), redispersion in 10 ml and final dialysis against ultrapure Milli-Q water for 72 h using tubes in cellulose membrane with a molecular weight cut-off of 12000 Da (Sigma-Aldrich).

CNC-DOX synthesis

Adsorption of doxorubicin hydrochloride (Sigma-Aldrich) was performed at different loadings, according to the following CNCs/DOX ratios: 10:1, 4:1 and 2:1. To a set of CNC aqueous suspension (10 ml, 0.5% w/V, 50 mg), 5 µl of triethylamine (Et_3N) and 5.0, 12.5 and 25 mg of DOX were added, respectively. The suspensions were stirred at RT for 24 h. The sample purification was attained through successive CNC-DOX precipitation in EtOH and centrifugation cycles (3200 g, 15 min). The pellets were re-suspended restoring a 0.5% w/V concentration and dialyzed against distilled water for 72 h. Blank experiments without Et_3N were also performed under the same conditions. The amount of DOX adsorbed onto the CNC surface was assessed by UV-Vis analysis, according to the method described by Jackson JK et al. [17], using a DOX calibration curve, measured at 480 nm, described by the equation: $y = 19.302x + 0.0109$ ($R^2 = 0.9991$).

Alexa Fluor 633 labelled CNCs

To a suspension of CNCs (0.5%, 25 ml), 1 mg of Alexa Fluor 633 hydrazide, bis(triethylammonium) salt (Life Technologies), and 200 µl of acetic acid were added. The mixture was let to react at RT in the dark. After 24 h, the mixture was dialyzed against distilled water for 1 week to remove the acetic acid and the non-reactive fluorophore [7].

CNC characterization

The ATR-FTIR spectra were performed with a Nicolet iS10 spectrometer (Thermo Scientific) equipped with an iTR Smart device (total scan 32, range 4000-800 cm^{-1}, resolution 2 cm^{-1}). The UV-Vis absorption spectra were collected with a UV-Vis spectrophotometer Evolution 300 (Thermo Scientific). ^{31}P-NMR spectra were recorded on 800 µl of sample in deuterated water, D_2O, with 1 µl of trimethylphosphate as internal standard and with 20 mg of CNCs-ALN by a Bruker Advance 500 MHz instrument at RT. Relaxation delay of 5 s was used between scans (90° pulse angle). Line broadening of 3 Hz was applied to FIDs before Fourier transform. For each spectrum, typically 1000 scans were accumulated. For AFM analysis, 50 µl of CNCs were immediately added onto freshly cleaved mica for 5 min, then washed and dried under nitrogen flow. AFM analysis was carried out on a Multimode AFM with a Nanoscope V system (Veeco/Digital Instruments, Mannheim, Germany) operating in tapping mode, using standard antimony (n) doped silicon probes (T, 3.5-4.5 µm; L, 115-135 µm; K, 20-80 N/m) (Bruker Corporation, Billerica, MA). Images were acquired in height and amplitude error and analyzed by Scanning Probe Image Processor (SPIP-version-5.1.6) data analysis package (five different, well-separated areas). DLS and ζ-potential measurements were performed using a Zeta Sizer Nano 3600 (Malvern) with an operating laser (λ=632.8 nm) and a backscattering angle of 173°. The data were processed by Zetasizer Software 7.03. The samples were prepared by diluting initial particles of stock solution 0.5% w/V in Milli-Q water to obtain a final concentration of 140 mg/L. Measurements were carried out at 25°C using a disposable cuvette. Three replicate measurements per sample were performed to establish measurement repeatability.

Release of DOX from CNCs at acidic pH

The release of drug from DOX-loaded CNCs was performed according to the following procedure: for each sample described above (CNCs/DOX ratio 10:1, 4:1 and 2:1), a set of 3 vials containing 1 ml of CNCs-DOX suspension and 4 ml of acetate buffer (pH 5.1, 0.05 M) was placed in a water bath set at 45°C and kept under magnetic stirring for 6, 24 and 48 h, respectively. Then, excess EtOH was added to the suspension to precipitate CNCs. After centrifugation (3200 g, 10 min), the

supernatant containing the released DOX was recovered, the solvent rotary evaporated and then the dried solid residue dissolved in 1 ml of a 1:1 H_2O/EtOH solution. The obtained solutions, further diluted by the 1:1 H_2O/EtOH solution, when necessary, were finally subjected to UV-Vis analysis to measure the amount of released DOX.

Animals

The Institute for Pharmacological Research "Mario Negri"-IRCCS adheres to the principles set out in the following laws, regulations, and policies governing the care and use of laboratory animals: Italian Governing Law (D.lgs 26/2014; Authorization n.19/2008-A issued March 6, 2008 by Ministry of Health); Mario Negri Institutional Regulations and Policies providing internal authorization for persons conducting animal experiments (Quality Management System Certificate – UNI EN ISO 9001:2015 – Reg. N°6121); the NIH Guide for the Care and Use of Laboratory Animals (2011 edition) and EU directives and guidelines (EEC Council Directive 2010/63/UE). The Statement of Compliance (Assurance) with the Public Health Service (PHS) Policy on Human Care and Use of Laboratory Animals has been recently reviewed (9/9/2014) and will expire on September 30, 2019 (Animal Welfare Assurance #A5023-01). This work was reviewed by IRCCS-IRFMN Animal Care and Use Committee (IACUC) and approved by the Italian "Istituto Superiore di Sanità" (code: 42/2016-PR). Mice were maintained under specific pathogen-free conditions at the Institute's Animal Care Facilities. They received food and water *ad libitum* and were regularly checked by a certified veterinarian who is responsible for animal welfare supervision and experimental protocol revision.

Treatment and optical imaging

In the biodistribution studies, 45 CD1 female mice (30 g) were enrolled. Animals were treated with CNC-SO_3^- (n=20), CNC-ALN (n=20) and saline for the vehicle group (n=5). For each CNC formulation, animals were randomly sacrificed at 4, 24, 48 and 96 h (n=5 for each time-point). Mice were intravenously injected with 20 mg/kg of CNC-SO_3^- or CNC-ALN. Fluorescence images were acquired *in vivo* and *ex vivo* with IVIS Lumina III imaging system combined to X-rays scanning

(Perkin Elmer). The acquisition parameters were: excitation filter range: 680 to 740 nm, emission filter: 790 nm. Spectral unmixing and image analysis were performed using Living Image 4.3.1 software. After the last *in vivo* scanning, animals were sacrificed by an overdose of ketamine (150 mg/kg) and medetomidine (2 mg/kg). Liver, kidneys, spleen, lungs, vertebral column, and hind legs were explanted for *ex vivo* imaging.

Histology

Cryostat sections from livers, kidneys and lungs of mice sacrificed at 4 and 96 h after treatment, were cut at 20 µm. The Hoechst-33258 (2 µg/ml in PBS, Molecular Probes) was used to label nuclei, whereas CNCs were detectable for the presence of Alexa Fluor 633. The sections were analyzed by Olympus Fluoview microscope with confocal system FV500 equipped with specific lasers λ_{exc} 405 nm for Hoechst-33258 and λ_{exc} 635 nm to visualize the signal associated with CNCs. The post-processing of images was carried out through Image J software. Lungs from animals sacrificed at 96 h after treatment (n=2 for each group) were fixed in 10% neutral buffered formalin (Bio-Optica) for 24 h, paraffin-embedded and sectioned at 4 µm thickness. Haematoxylin-Eosin staining (H&E) was carried out and sections were visualized through a light microscope (Olympus BX61VS).

Cellular uptake

Human mammary adenocarcinoma cells, MDA-MB-231, were used to perform the uptake assay. Cells were cultured in DMEM (Sigma-Aldrich) complemented with 10% FBS (Sigma-Aldrich), 2 mM L-glutamine, and 100 U penicillin/0.1 mg/ml streptomycin, and maintained at 37°C in 5% CO_2. Cells were seeded at a density of 15000 cells/cm^2 in 24-well plates, incubated with the different compounds, and the uptake efficiency was observed at 6, 24 and 48 h. CNC-SO_3^- and CNC-ALN were incubated at 70 µg/ml of CNCs. In additional experiments, CNC-DOX and free DOX were used at 0.5 µM of DOX. After incubation, cells were washed and fixed with 4% paraformaldehyde (Bio-Optica) for 45 min. The nuclei were stained with Hoechst-33258 (2 µg/ml in PBS) for 10 min. Cells were analyzed with Olympus Fluoview microscope BX61 with confocal

system FV500 (λ_{exc} 405 nm for Hoechst-33258; λ_{exc} 532 nm to visualize DOX; λ_{exc} 635 nm to visualize Alexa Fluor 633-labelled CNCs). Image quantification was made through Image J software and for each experimental group 10 acquisitions were captured with 20x objective. The values express the ratio between the signal associated with CNCs (area) and the cell number for each field of view.

Cellular viability

Murine macrophage cell line, RAW 264.7, human pre-osteoclasts (OC) derived from peripheral blood mononuclear cells (PBMC) and MDA-MB-231 were employed to assess cellular viability. To obtain OC, PBMC were isolated from three human buffy coats obtained from the blood bank, by gradient centrifugation (Ficoll-Hypaque, GE Healthcare) at 900 g for 30 min, as described elsewhere [18]. Then, PBMC were pooled and washed twice with PBS centrifuging at 760 g for 10 min. PBMC were seeded in 96-well plates in α-MEM containing 20% FBS, 25 ng/ml M-CSF and 50 ng/ml RANK-L (Life Technologies) to be differentiated towards OC. The non-adherent cells were removed three days later by medium renewal. Then, the medium was refreshed every 72 h for 7 days. For both RAW 264.7 and MDA-MB-231, DMEM was used and cells were seeded in 96-well plates. RAW 264.7 and pre-OC were treated with CNC-SO_3^-, CNC-ALN, and free ALN at four doses of ALN (10^{-4}; 10^{-6}; 10^{-8}; 10^{-10} M) for 48 h. MDA-MB-231 cells were treated with CNC-DOX and free DOX at two doses (0.5 and 2 μM) for 6, 24, and 48 h. Cell viability was evaluated by CellTiter 96® AQueous One Solution Cell Proliferation Assay kit (Promega), read in absorbance at 490 nm. Data are presented as proportional viability (%) by comparing the treated group with the untreated cells, the viability of which is assumed to be 100%.

Data Calculation and Statistical Analysis

All data are expressed as mean ± standard error (SEM). Two-way analysis of variance (ANOVA), followed by Sidak's post-test analysis, was used. All statistical analyses were done using the GraphPad Prism version 6.00 for Windows (Graph-Pad Software, San Diego, CA).

Results

Design Synthesis and Characterization of Fluorescently Labelled CNCs

Due to the insertion of half sulfate esters on the CNC surface during the extraction procedure, these samples were named CNC-SO_3^-. The half sulfate esters improved the colloidal stability by a ζ-pot equal to -33.0mV and their amount was determined by conductometric titration and found to be 0.17 mmol/g, confirming our previous study [19]. Then, the primary hydroxyl groups on the nanocrystal surfaces were modified in carboxylic acids through an oxidation reaction mediated by TEMPO, obtaining CNC-COOH. Finally, the nanocrystal surface was further modified with sodium alendronate exploiting the carboxylic groups by EDC coupling with the free amine group of the drug itself (CNC-ALN). To follow the fate of the CNCs *in vitro* and *in vivo* and to assess their biodistribution, a fluorescent tag (Alexa Fluor 633 hydrazide) was attached to the reducing end of CNCs. It was already demonstrated that the Alexa labelling did not modify the CNCs superficial properties [7]. The amount of Alexa bonded to different preparations was kept constant and confirmed by UV-Vis spectroscopy [7]. Figure 1A summarizes the main steps of the synthesis of CNC-ALN.

CNC characterization

Before biological studies, both CNC-SO_3^- and CNC-ALN were characterized to measure the concentration of CNCs in solution (%, w/V) and to assess their main physicochemical parameters, such as size, polydispersity index and surface charge by DLS (Figure 1B). It is noteworthy that the CNC-ALN synthetic procedure led to little, but well detectable modifications of these parameters. However, these changes were somehow expected in case of multi-step processes.

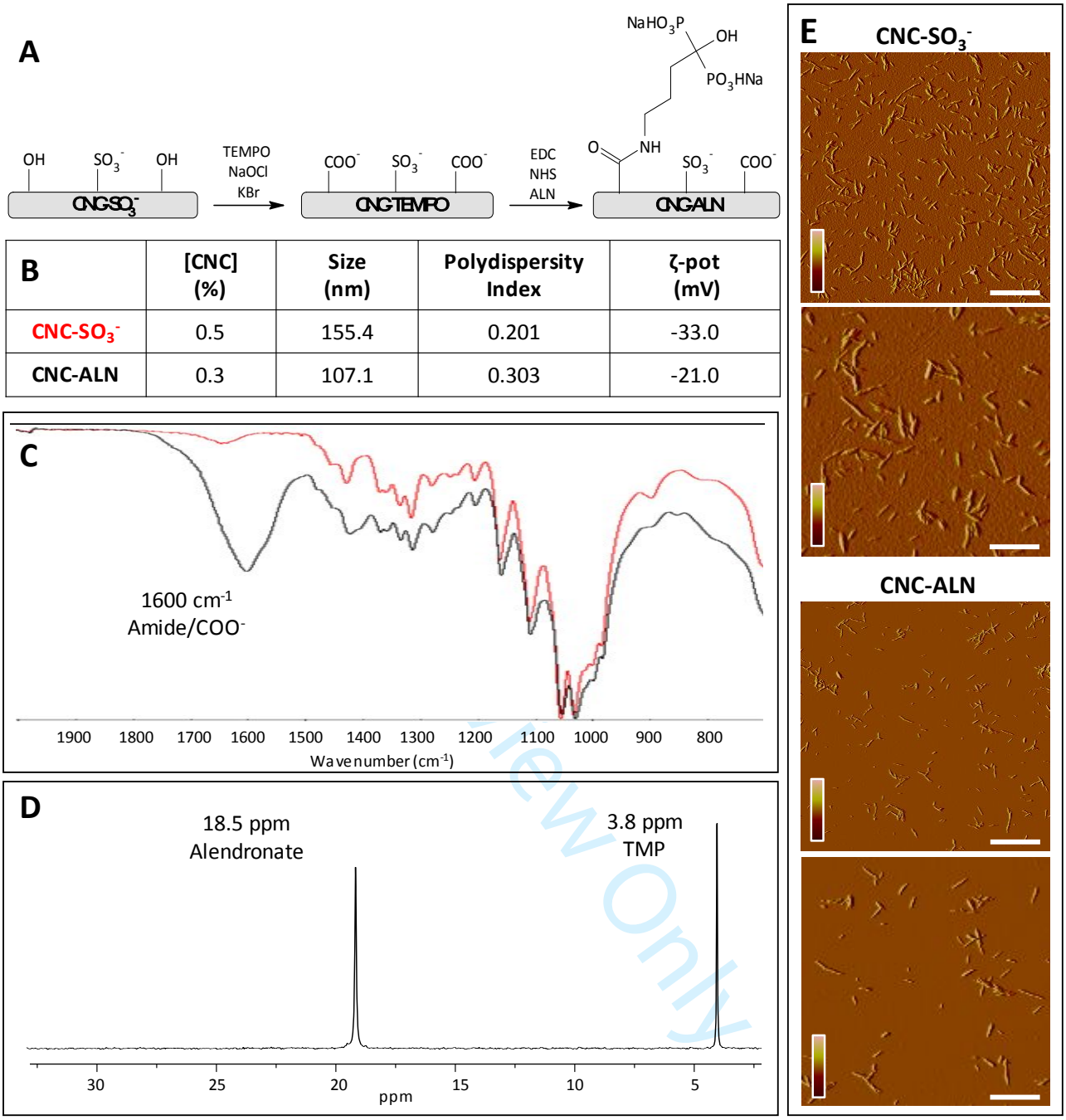

Figure 1: A) Schematic reaction summarizing the multi-step synthesis of the conjugate Cellulose Nanocrystals (CNC-SO_3^-) with Alendronate (CNC-ALN); B) Table summarizing the main physicochemical properties of CNCs determined by DLS; C) FT-IR spectra of CNC-SO_3^- (red) and CNC-ALN (black); D) Representative ^{31}P-NMR spectrum of CNC-ALN. E) Representative tapping mode of AFM images as determined by amplitude error data of CNC-SO_3^- and CNC-ALN after incubation in distilled water. Two different magnifications were reported (for both formulations, upper panels: scale bar 2 µm; lower panels: scale bar 1 µm). Scale color amplitude error: 100/-60 mV.

To qualitatively follow the modification reactions, FT-IR analyses were performed on CNC-SO_3^- and CNC-ALN, as reported in Figure 1C. From the spectra, it was possible to highlight a new band at around 1600 cm^{-1} related to the carboxylate group generated by TEMPO oxidation and its

conversion in amide bond by the EDC coupling with ALN (the two bands are partially overlaid). Another diagnostic modification was the disappearance of the small band at around 900 cm^{-1} related to the primary alcoholic group in C6 position of the anhydroglucan unit, likely due to the selective oxidation promoted by TEMPO. To quantitatively determine the efficacy of the ALN conjugation to CNCs in terms of mmol drug/g of CNCs, ^{31}P-NMR analyses were carried out. Figure 1D reports the spectrum of the synthesized CNC-ALN. Two peculiar peaks were detected: the first at 18.5 ppm refers to the sodium alendronate, the second at 3.8 ppm corresponds to the inner control, the trimethylphosphate (TMP). A spectrum of free ALN was performed as control (data not reported). A peak at 18.5 ppm with a typical chemical shift of the bisphosphonates was detected. In the CNC-ALN spectrum, the first peak evidenced that ALN was actually linked to CNCs and, based on the TMP intensity, that its concentration was 0.77 mmol/g of CNCs (with a loading efficiency of 17%). Finally, to visualize the newly synthesized CNCs, AFM experiments were performed. Figure 1E shows representative images of both CNC-SO_3^- and CNC-ALN at two different magnifications. A rod-like shape was seen for both formulations. In addition, CNCs were monodispersed and similar in size: 7-10 nm thickness and 5-20 nm height. Moreover, two main particle length distributions were observed: 100-150 nm (60%) and 200-350 nm (40%).

CNC-DOX characterization

The amount of DOX (expressed in mg/g of CNCs) bound to the NPs increased as the CNC/DOX ratio (expressed by w/w) decreased, as shown in Figure 2A. Specifically, the data varied from 20 mg/g at 10:1 ratio to 80 mg/g of DOX per g of CNC at 2:1 ratio. The binding efficiency (BE) was roughly 15-20%. Figure 2B shows the cumulative DOX release for CNC-SO_3^- bounded with DOX at different ratios at pH 5.1. In this condition, the % drug released increased with the DOX bounded. According to previous studies, the desorption mechanism was related to the higher solubility of DOX at acidic condition [20]. The maximum release was found in 2:1 loading reaching 80% of DOX at 48 h.

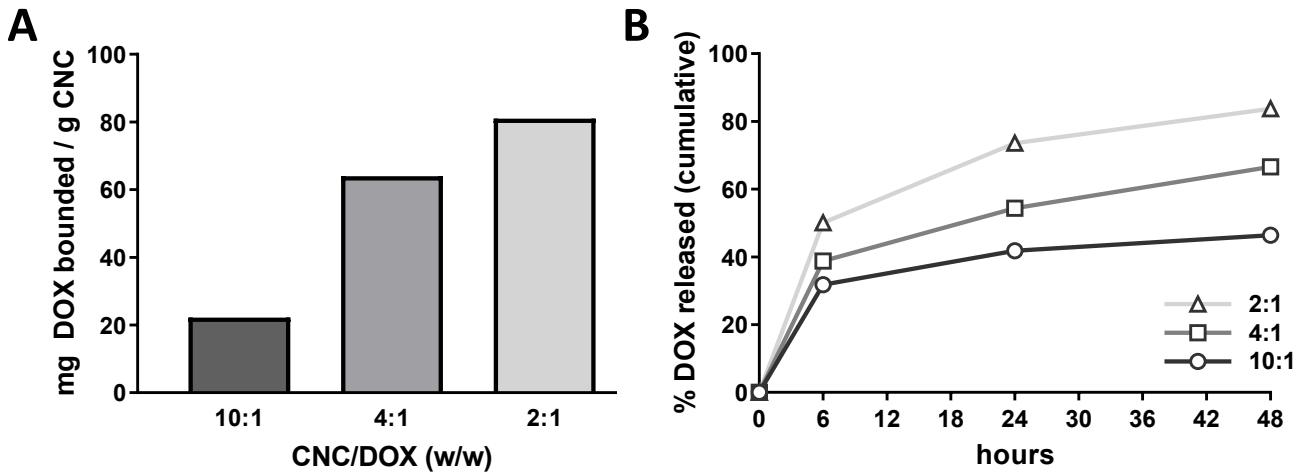

Figure 2: A) DOX loadings (expressed in mg of DOX bounded to 1 g of CNC specimen) to CNC-SO_3^- depending on the CNC/DOX ratio; B) cumulative DOX release in % at pH 5.1 for the CNC-SO_3^- preparation at different loading.

CNC biodistribution

The biodistribution of fluorescently labelled CNC-SO_3^- and CNC-ALN was analyzed in healthy mice by optical imaging technique. Representative whole-body images of vehicle and CNC-treated mice at 4 h are shown in Figure 3A. Mice treated with CNC-SO_3^- confirmed an intense fluorescence diffused in abdominal and thoracic regions. Moreover, a well detectable signal was observed in hind legs. A higher magnified picture (bottom panel) confirmed the presence of signal along bones and joints. CNC-ALN showed a similar pattern of fluorescence and maintained a peculiar tropism toward hind legs. In both experimental groups, a progressive reduction of the signal was detected until 96 h, without difference in their kinetics (data not shown). To better evaluate the tropism of CNCs to the skeletal system, an *ex vivo* study was carried out by scanning isolated bones at selected time points. Figure 3B shows vertebral columns, femurs, tibias and distal hind legs of animals sacrificed 4 h after the administration of the vehicle, CNC-SO_3^- or CNC-ALN. A strong and homogeneous signal was observed in bones in both CNC groups, with the highest intensity in the vertebral columns and distal hind legs. The longitudinal quantification of the signal in bones of treated animals is shown in Figure 3C. Vertebral columns and distal hind legs had a higher level of signal compared to the femurs and tibias. In the vertebral column, a high level of signal was observed 4 h after administration with a drastic reduction within the first 24 h in both groups. In

distal hind legs, the trend of the fluorescence was similar to that measured in vertebral columns. CNC-ALN treated mice showed a milder reduction of fluorescence at two later time points.

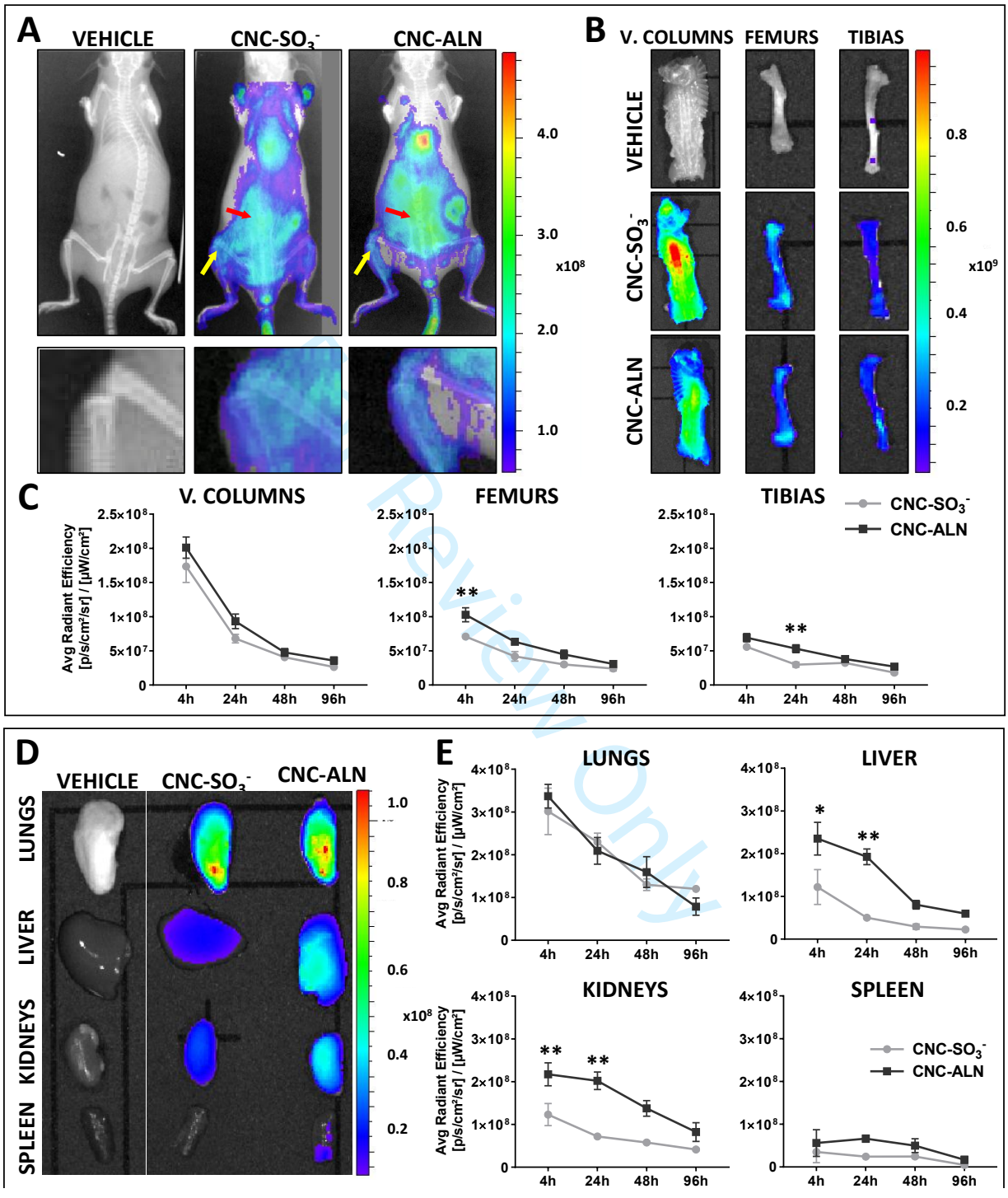

Figure 3: A) *In vivo* optical and X-rays imaging of the vehicle-, CNC-SO_3^-- and CNC-ALN-treated mice 4 h after IV administration. In upper panels, representative total body scans are reported. In the lower panels, higher magnified images of the knee joint are depicted. B) Representative pictures of the vertebral columns, femurs, and tibias of mice treated with vehicle, CNC-SO_3^- or CNC-ALN 4 h after treatment. C) Diagrams showing the trend of signal intensity in bones of mice treated with CNC-SO_3^- or CNC-ALN. **D**) *Ex vivo* optical imaging of lungs, liver, kidneys and spleen from vehicle-, CNC-SO_3^-- and CNC-ALN-treated animals sacrificed 4 h after IV administration. E) Diagrams showing the trend of signal intensity in organs from animals treated with CNC-SO_3^- and CNC-ALN. A, B, D) The fluorescence signal intensity, measured as radiant efficiency, is shown as a pseudo-color scale bar. The

pseudo-color scale bar is consistent for all images to show relative changes of biodistribution over time. C, E) All data are expressed as mean ± SEM and analyzed by Two-way ANOVA followed by Sidak Post-hoc test. *<0.05, **<0.005 CNC-SO_3^- vs. CNC-ALN. The overall influence of time for all the bones, lungs, livers and kidneys is p<0.0001.

Ex vivo imaging of lungs, liver, kidneys, and spleen of mice sacrificed 4 h after injection of vehicle, CNC-SO_3^- or CNC-ALN is shown in Figure 3D. Both CNCs had a high tropism toward the lungs and showed low accumulation in the spleen. Interestingly, a low accumulation of CNC-SO_3^- was found in the kidneys and liver, while the functionalization with ALN led to an increased CNCs accumulation at 4 and 24 h after injection in these organs. Over time an almost linear decay of the signal was observed in all organs of both CNC-SO_3^- or CNC-ALN-treated mice, although the signal was still detectable 96 h after treatment (Figure 3E).

To better characterize the localization of CNCs, confocal microscopy of liver, kidneys, and lung section was carried out in mice sacrificed 4 or 96 h after administration (Figure 4). In the liver sections of CNC-ALN-treated mice, the fluorescent signal was detected at both time points (4 and 96 h) multifocally at the level of cells localized in the parenchyma along the sinusoids. Differently, in CNC-SO_3^--treated mice the signal was localized at the blood vessel walls only at 4 h after treatment, and no signal was observed in the parenchyma at both time points. A marked accumulation of CNCs in blood vessel walls was observed in the kidneys of mice treated with CNC-SO_3^- and CNC-ALN at both time points. No accumulation was observed in the other renal structures. In the lungs, an intense and protracted fluorescence signal was detected in both the experimental groups with similar distribution and intensity until 96 h. The signal appeared as continuously distributed along the alveolar structures and was detected also at blood vessel walls and at the periphery of the bronchioles.

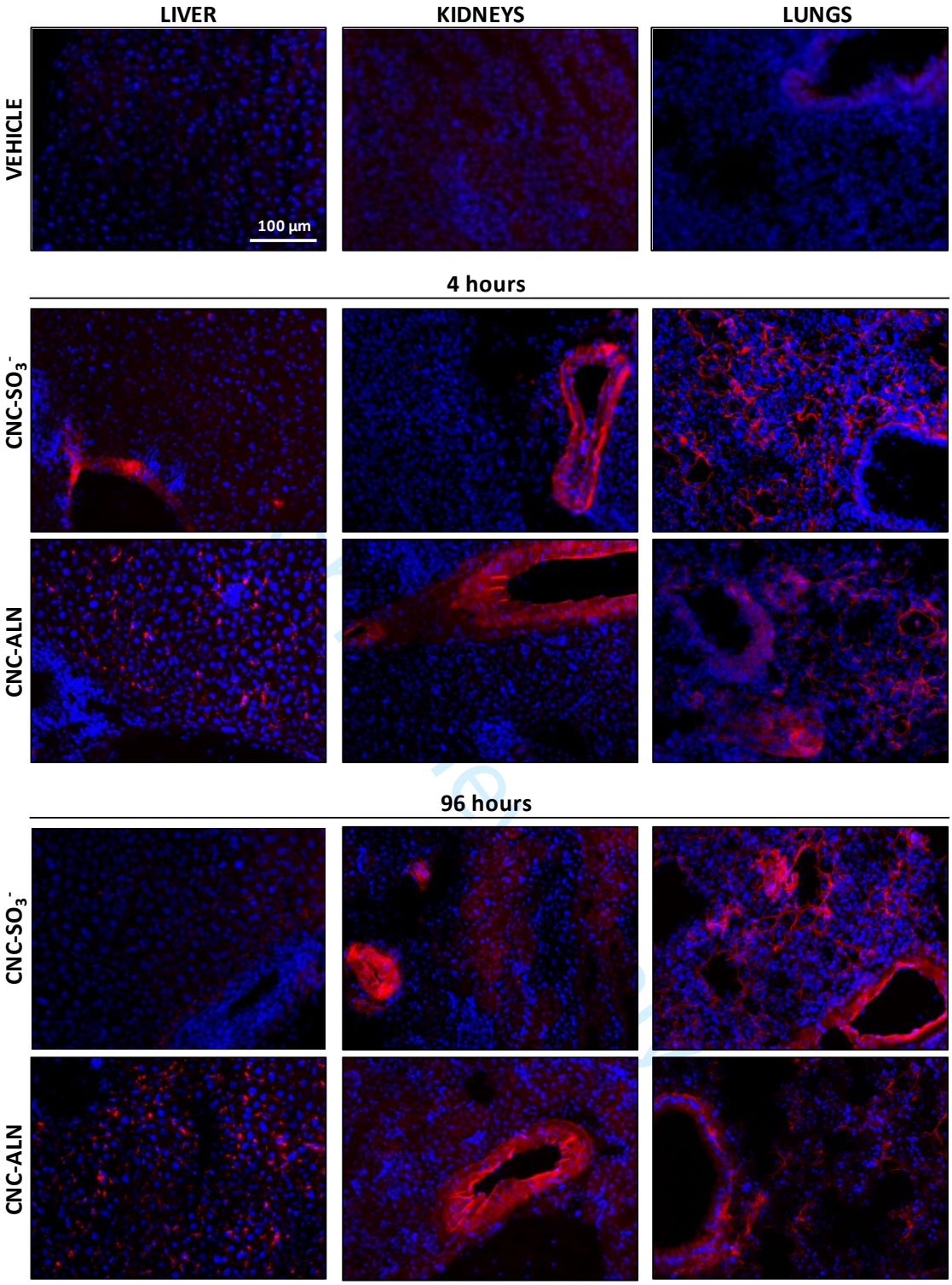

Figure 4: Representative pictures showing the tissue distribution of CNC-SO_3^- or CNC-ALN (red signal) in liver, kidneys, and lung 4 and 96 h after treatment. In the upper panel, the sections were excited with the laser associated with the excitation peak of CNCs, but as expected, no signal was revealed. Hoechst-33258 staining (blue dots) has been used to stain the nuclei.

No treatment-related histopathological changes were observed at 96 h in the lungs of both CNC-SO_3^- and CNC-ALN-treated mice (Figure 5).

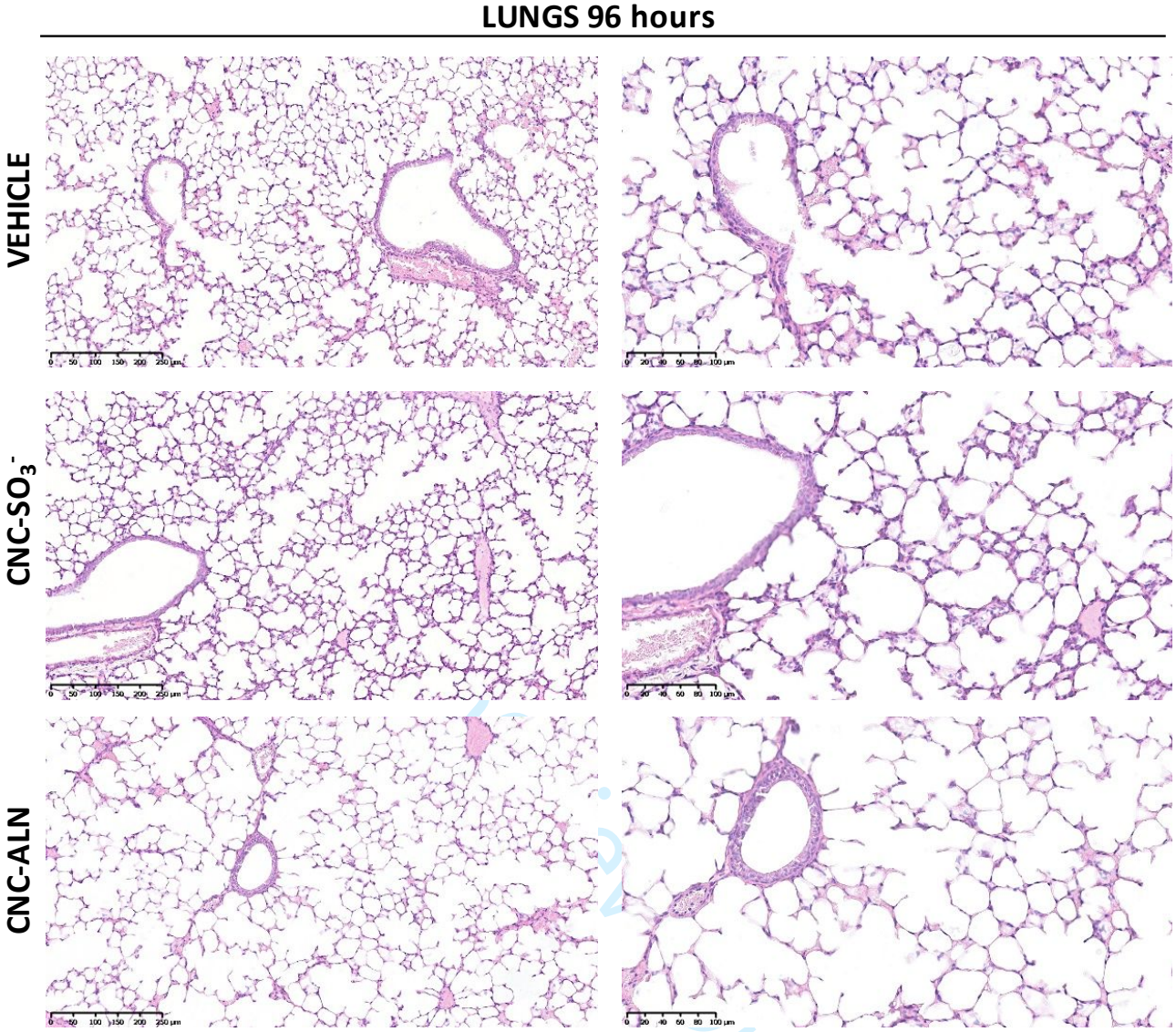

Figure 5: Histological evaluation by Haematoxylin and Eosin staining of lung tissues of mice treated with vehicle, CNC-SO_3^- and CNC-ALN and sacrificed 96 h after the treatment.

Cell target interaction

Figure 6A shows the process of internalization of both CNC-SO_3^- and CNC-ALN in MDA-MB-231 after 24 h of incubation. Lower magnification images revealed an almost heterogeneous penetration of CNCs. As expected, CNC-SO_3^- exclusively localized in the cytoplasm, with the spotty staining suggesting their clusterization in vesicles. No relevant change of intracellular localization was observed when cells were incubated with CNC-ALN. On the contrary, the uptake efficiency (expressed as the ratio between the red signal area and nuclei, normalized to the single-cell) was higher in CNC-ALN-treated cells (Figure 6B).

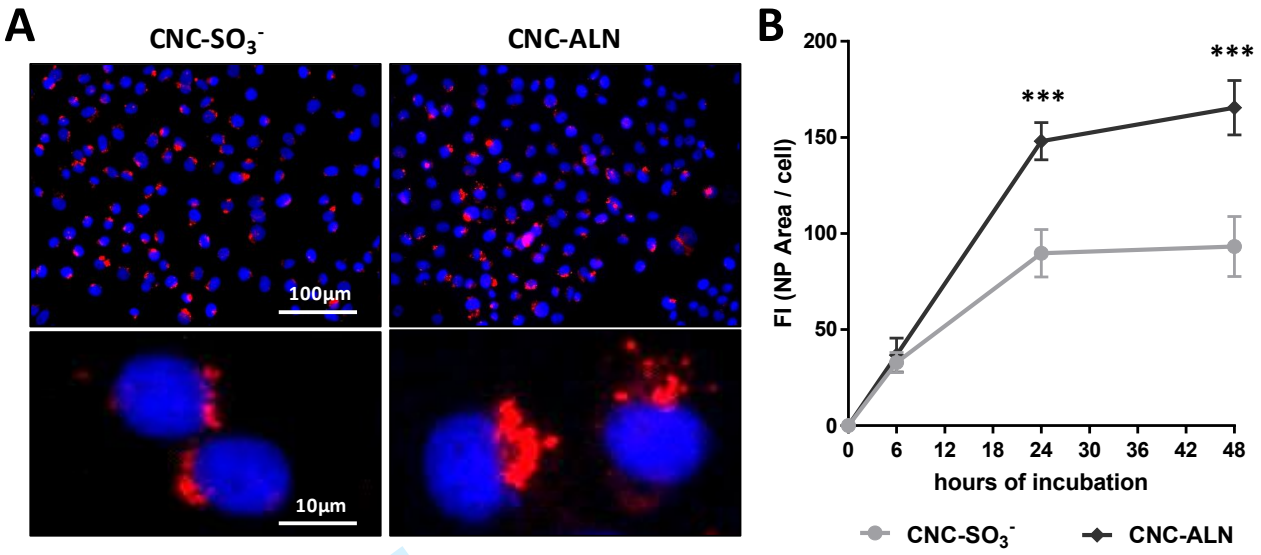

Figure 6: A) Representative images showing the presence of both CNC-SO_3^- and CNC-ALN in MDA-MB-231 cells 24 h after incubation. In the upper panel, a field of view with a quite large number of cells and a single cell staining are depicted in the upper and lower panel, respectively. CNCs are visualized in red (Cy5 signal) and nuclei in blue (Hoechst-33258 staining). B) Quantification of cellular uptake 6, 24 and 48 h after treatment. The data are expressed as mean ± SEM and analyzed by Two-way ANOVA followed by Sidak Post-hoc test. ***<0.0005 CNC-SO_3^- vs. CNC-ALN. The overall influence of time is p<0.0001.

After evaluating the internalization efficiency of both CNC-SO_3^- and CNC-ALN, the loading of ALN into CNCs was analyzed to assess a potential decrease of its therapeutic activity. To do this, the effect of free ALN or ALN linked to CNCs was evaluated in both RAW 264.7 and pre-OC at different doses after 48 h of incubation (Figure 7).

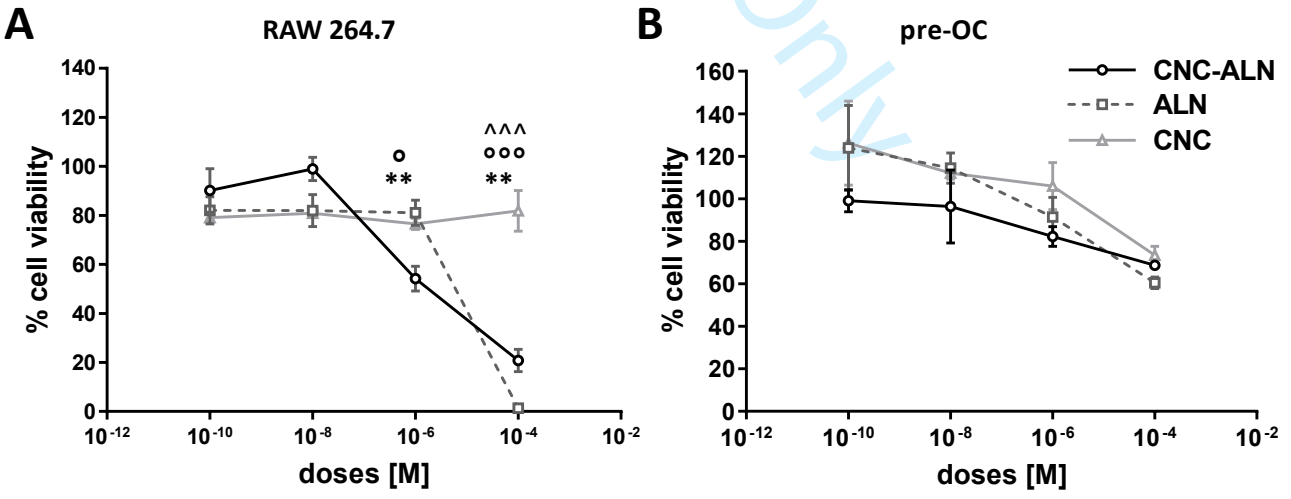

Figure 7: MTS assay performed incubating A) RAW 264.7 and B) pre-OC with ALN free or linked to CNCs at the following concentrations (10^{-10}, 10^{-8}, 10^{-6}, 10^{-4} M) for 48 h of incubation. The same amount of CNC linked to ALN was incubated without the drug to evaluate the effect of CNC alone. Data are expressed as mean ± SEM and analyzed by Two-way ANOVA followed by Sidak Post-hoc test. *<0.05, **<0.005, ***<0.0005. *ALN vs. CNC-ALN, °CNC vs. CNC-ALN, ^CNC vs. ALN.

Figure 7A clearly shows that both free ALN and CNC-ALN were able to reduce macrophage viability at higher doses than 10^{-6} M. Not surprisingly, CNCs alone did not affect cell viability. As shown in Figure 7B, a dose-dependent trend was observed in pre-OC. At lower doses (10^{-10} and 10^{-8} M), CNC-ALN yielded lower cell viability compared to CNCs and free ALN, although these differences were not statistically significant. At higher doses, CNC-ALN and ALN showed comparable effects. The cytotoxic effect of CNCs alone increased at the highest concentration.

Finally, the effect of CNCs linked to anticancer agents (DOX) was tested in MDA-MB-231 cells. Figure 8A shows the cellular uptake of free DOX or DOX linked to CNCs also exploiting the fluorescence of the drug ($\lambda_{emission}$ 591 nm). Data demonstrated that free DOX localized into the nucleus, the target subcellular organelle of the drug. Notably, the violet signal in the higher magnified picture clearly demonstrated the co-localization with the nucleus. On the other hand, only a mild release of DOX from CNCs was detectable at this time point. In fact, the spotted red fluorescent signal showed some molecules of DOX still attached to CNCs, confined and clustered into endocytic vesicles. The diagram in Figure 8B shows that: i) a time-dependent effect was observed independently of the type of formulation; ii) in both formulation the DOX concentration played a role in reducing the overall survival 24 h and 48 h after treatment; iii) the effect of concentration was markedly higher for the nanoformulation compared to DOX alone.

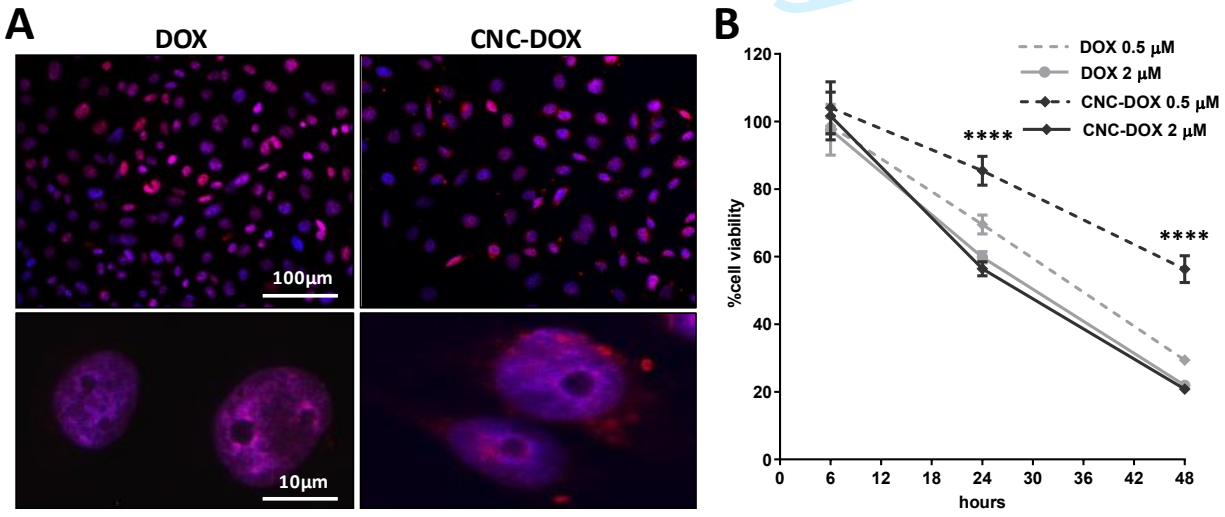

Figure 8: A) Representative confocal microscopy images showing internalization of 0.5 µM of DOX free or conjugated to CNCs (red signal represents DOX autofluorescence) in MDA-MB-231 cells after 24 h of incubation. Two levels of magnification were

reported. Nuclei are visualized in blue (Hoechst-33258 staining) and DOX in red. B) Diagram showing the toxicity of DOX free or conjugated to CNCs in MDA-MB-231 cells, at two different doses (0.5 and 2 μM). Data are represented as mean ± SEM and analyzed by Two-way ANOVA followed by Sidak Post-hoc test. ****<0.0001 DOX vs. CNC-DOX at 0.5 μM. No significant difference was found comparing DOX vs. CNC-DOX at 2 μM. The overall influence of time is p<0.0001.

Discussion

Osteoporosis and breast cancer-derived bone metastases are increasing in incidence, morbidity and mortality in women [21,22]. In spite of the *in vitro* evidence of specific pharmacological tools for both therapies, there are several hurdles that dramatically reduce their efficacy in patients. They mainly include low stability, short plasmatic half-life, poor bioavailability in bones and hazardous accumulation in off-target organs [10–13,23].

The present study was therefore aimed at developing delivery systems to improve the targeting of either anti-cancer or anti-osteoporosis drugs, in the attempt to somehow overcome the aforementioned pharmacokinetic limitations. To this aim, we synthesized innovative nanocarriers based on CNC backbone. Our *in vivo* results confirmed that the peculiar physicochemical properties of CNCs greatly increased the ratio of bone/filter organs. Indeed, CNCs due to their elongated shape and thin size establish direct contact with the vessel walls and escape from the bone microvasculature, which favors the interaction with the cationic surface of the bone matrix, by their negative charges [3,7,24]. The reliability of our tracking derived from our ability to covalently link both ALN and the fluorescent dye to CNCs. This strongly reduced the risks of biological elution of the cargo and the dye after intravenous administration and/or incubation in medium [25].

Our experimental evidence demonstrated that a specific tropism among the different bones occurred. The main tropism was detected in the vertebral column and the femoral epiphysis. This suggested a different uptake between cancellous and cortical bone. In particular, the greater uptake of cancellous bone could be related to the bone turnover and blood flow, rather than to the bone density. Moreover, ALN linkage did not modify this peculiar interaction, as a significant increase of signal was seen in femurs (4 h) and in tibias (24 h) of CNC-ALN compared to CNC-SO^{3-} treated

mice. No difference in the overall trend was observed. However, there was a significant time-dependent reduction. We also demonstrated that the presence of ALN did not induce any perturbation to CNC peculiar tropism. Similarly to other negatively charged nanotubes and nanorods, CNCs poorly accumulated in the liver and spleen [3,26]. However, a significant increase of uptake from resident liver macrophages was found in animals treated with CNC-ALN compared to those receiving CNC-SO_3^-. Although such behavior could be ascribed to several factors, further *in vitro* experiments, showing the same difference among CNC-ALN and CNC-SO_3^- in terms of internalization in RAW 264.7, led us to hypothesize that the higher stealthiness of CNC-SO_3^- can be due to a lower bioavailability. Our characterization revealed that, during the process of CNC-ALN formation, there was a significant shortening of the nanocrystal. It is therefore possible to argue that, as previously reported, a margination of nanoparticles in capillaries as a function of their size and shape can occur [27]. It was quite reasonable that intravenously injected extremely thin and negatively charged nanoparticles could rapidly interact with the renal tubular system; also in this case CNC-ALN seemed to better interact with the organ parenchyma. Overall, the nanoparticle accumulation in the lungs, in this case without any difference between the two treatments, is associated with a very large size or the occurrence of aggregations. However, fluorescent images highlighted the presence of stretched structures, mainly associated with endothelial cells. This tropism could be of interest for the development of other targeted systems against pulmonary disorders. However, to this aim, although no evidence of relevant histological alterations was observed in mice sacrificed 4 days after the treatment, a deeper investigation after a repeated treatment should be carried out.

One of the main hurdles in the clinical management of patients assuming bisphosphonates is the poor oral absorption. Therefore, the parenteral administration has been taken into consideration in recent years. Bisphosphonate pharmacokinetics shows a rapid and homogenous distribution in bone and soft organs, in particular kidneys and spleen, but they are also rapidly cleared by renal filtration with a plasmatic half-life of 90 min [28,29].

Our data showed that the linkage with CNC enables us to maintain ALN in different organs, including bones for a long time. In terms of efficacy, the combination of CNCs and ALN seemed to slightly increase the cytotoxic effect of ALN on osteoclast precursors, at least at lower doses. The lack of a clear effect of both ALN and CNC-ALN on pre-OC may depend on the short pre-differentiation period chosen to induce primary PBMC into OC. Additionally, cytotoxicity might not be the primary mechanism of action of ALN, which could exert a more relevant action on osteoclast differentiation [30].

Another important aim of this study was the adsorption of the anticancer agent DOX into CNCs. It has been already demonstrated that the administration of DOX by liposomes dramatically reduces the side effects and the off-targeting [31]. However, this strategy does not improve the ability to reach the bone target. In this context, we found that the use of charged particles (negatively for CNCs) to bind and release basic drugs (such as DOX) is well established [32]. To avoid modifications of the CNC surface and maintain a good colloidal suspension stability and bone targeting, a strategy based on surface adsorption has been undertaken [17,32]. The CNC-DOX preparations were not characterized in term of physicochemical properties, anyways only a limited decreasing of colloidal stability was observed (directly related to the DOX bounded) in agreement with a reported decreasing of ζ-potential [17,20]. The mechanism of adsorption was based on hydrophobic, hydrogen-bond and electrostatic interactions [20,33]. It is important to underline that, in contrast to previous studies, we found a lower binding efficacy [17]. However, this reduction was counterbalanced by a better purity of our nanocarrier through the deeper washing procedure adopted. The observed difference seemed to play an important role also during drug release investigations, where CNCs showed a faster but more controlled release than that reported in the literature [17]. Notably, the presence of the CNC backbone did not modify the well-established effect of DOX, even if a slight decrease of the cytotoxicity was observed due to the slow penetration of the drug when incubated as nanoformulation. It is well known that the interest of nanoparticles in medicine has emerged from their ability to reduce the side effects and therefore to

increase the therapeutic index of DOX [31]. In this context, the efficacy of CNC-DOX against breast cancer cells and the overall ability of CNCs to bind bones represent an added value to improve the pharmacotherapy in breast-derived bone metastases.

Conclusions

The main innovative hallmark of nanomedicine is the possibility to improve organ specificity of an extended range of drugs, therefore reducing side effects and risks [34]. Nanocellulose possesses diverse characteristics different from traditional materials, including peculiar size and shape, crystallinity, high specific surface area, surface chemical reactivity, biocompatibility, lack of toxicity and relatively low cost, making it an interesting nanomaterial for biomedical applications [35,36]. The functionalization reactions can also be extended to other chemical compounds, as for ALN and DOX, for future development of CNCs as therapeutic agents in severe bone-related diseases, in addition to osteoporosis and bone metastases.

Summary point.

- Alendronate (ALN) and Doxorubicin (DOX) were conjugated to CNC backbone to reduce their off-target organ accumulation and to improve their therapeutic efficacy.
- Chemical coupling of ALN and CNC was achieved through an amide bond exploiting an oxidation reaction. The loading of DOX was achieved through direct adsorption of the drug on CNC-SO_3^-.
- *In vivo* and *ex vivo* imaging studies demonstrated a specific tropism of CNC nanoformulations among the different bones for a long time.
- ALN linkage did not modify the CNC behavior, nevertheless the liver and kidney accumulation resulted slightly higher than CNC alone.
- CNC-ALN shows a dose and time-dependent trend on macrophage and pre-osteoclast viability.

- CNC-DOX did not modify the cytotoxic effect of DOX, even if at low dose the nanoformulation decreased DOX activity due to the slow penetration of the drug.

References

Papers of special note have been highlighted as: • of interest; •• of considerable interest.

1. Ventola CL. Progress in nanomedicine: approved and investigational nanodrugs. *P T*. 42(12), 742–755 (2017).

2. Farokhzad OC, Langer R. Impact of nanotechnology on drug delivery. *ACS Nano*. 3(1), 16–20 (2009).

3. Blanco E, Shen H, Ferrari M. Principles of nanoparticle design for overcoming biological barriers to drug delivery. *Nat Biotechnology*. 33(9), 941–951 (2015). •

• This study clearly demonstrates that nanoparticle size, shape and surface charge dictate the biodistribution.

4. Faria M, Björnmalm M, Thurecht KJ, *et al.* Minimum information reporting in bio–nano experimental literature. *Nat Nanotechnology*. 13(9), 777–785 (2018). •

• This study presents a "minimum reporting standard" for studies investigating bio-nano interactions.

5. Hirabayashi H, Fujisaki J. Bone-specific drug delivery systems: approaches via chemical modification of bone-seeking agents. *Clin Pharmacokinet*. 42(15), 1319–1330 (2003).

6. Habibi Y, Lucia LA, Rojas OJ. Cellulose nanocrystals: chemistry, self-assembly, and applications. *Chemical Reviews*. 110(6), 3479–3500 (2010).

7. Colombo L, Zoia L, Violatto MB, *et al.* Organ distribution and bone tropism of cellulose nanocrystals in living mice. *Biomacromolecules*. 16(9), 2862–2871 (2015). ••

•• This study proves the ability of cellulose nanocrystals to interact with bones, exploiting the chemical interaction between the $Ca^{(2+)}$ of the bone matrix and the active surface of negatively-charged nanocrystals.

8. Poole KE, Compston JE. Bisphosphonates in the treatment of osteoporosis. *BMJ*. 344, e3211–e3211 (2012).

9. Sledge GW, Neuberg D, Bernardo P, *et al.* Phase III trial of doxorubicin, paclitaxel, and the combination of doxorubicin and paclitaxel as front-line chemotherapy for metastatic breast cancer: an intergroup trial (E1193). *Journal of Clinical Oncology*. 21(4), 588–592 (2003).

10. Perazella MA, Markowitz GS. Bisphosphonate nephrotoxicity. *Kidney Int.* 74(11), 1385–1393 (2008).

11. Kennel KA, Drake MT. Adverse effects of bisphosphonates: implications for osteoporosis management. *Mayo Clin. Proc.* 84(7), 632–637; quiz 638 (2009).

12. Swain SM, Whaley FS, Ewer MS. Congestive heart failure in patients treated with doxorubicin: a retrospective analysis of three trials. *Cancer*. 97(11), 2869–2879 (2003).

13. Singal PK, Iliskovic N. Doxorubicin-induced cardiomyopathy. *N. Engl. J. Med.* 339(13), 900–905 (1998).

14. Barana D, Salanti A, Orlandi M, Ali DS, Zoia L. Biorefinery process for the simultaneous recovery of lignin, hemicelluloses, cellulose nanocrystals and silica from rice husk and Arundo donax. *Industrial Crops and Products*. 86, 31–39 (2016).

15. Saito T, Isogai A. Tempo-mediated oxidation of native cellulose. The effect of oxidation conditions on chemical and crystal structures of the water-insoluble fractions. *Biomacromolecules*. 5(5), 1983–1989 (2004). •

• This study explains the procedure to functionalize cellulose nanocrystals, through TEMPO-mediated oxidation

16. Huang C-F, Chen J-K, Tsai T-Y, Hsieh Y-A, Andrew Lin K-Y. Dual-functionalized cellulose nanofibrils prepared through TEMPO-mediated oxidation and surface-initiated ATRP. *Polymer*. 72, 395–405 (2015). ••

•• This study explains the procedure to functionalize cellulose nanocrystals, through TEMPO-mediated oxidation

17. Letchford, Jackson, Wasserman B, Ye, Hamad W, Burt H. The use of nanocrystalline cellulose for the binding and controlled release of drugs. *International Journal of Nanomedicine*. 6, 321-330 (2011).

18. Bongio M, Lopa S, Gilardi M, Bersini S, Moretti M. A 3D vascularized bone remodeling model combining osteoblasts and osteoclasts in a CaP nanoparticle-enriched matrix. *Nanomedicine*. 11(9), 1073–1091 (2016).

19. D'Orazio G, Munizza L, Zampolli J, *et al.* Cellulose nanocrystals are effective in inhibiting host cell bacterial adhesion. *Journal of Materials Chemistry B*. 5(34), 7018–7020 (2017).

20. Akhlaghi SP, Tiong D, Berry RM, Tam KC. Comparative release studies of two cationic model drugs from different cellulose nanocrystal derivatives. *European Journal of Pharmaceutics and Biopharmaceutics*. 88(1), 207–215 (2014). ••

•• This study shows the desorption mechanism to load cellulose nanocrystal with model drug compounds.

21. Black DM, Rosen CJ. Postmenopausal osteoporosis. *New England Journal of Medicine*. 374(21), 2096–2097 (2016).

22. Coleman RE. Clinical features of metastatic bone disease and risk of skeletal morbidity. *Clin. Cancer Res.* 12, 6243s–6249s (2006).

23. Cheng H, Chawla A, Yang Y, *et al.* Development of nanomaterials for bone-targeted drug delivery. *Drug Discovery Today*. 22(9), 1336–1350 (2017).

24. Soares AP, do Espírito Santo RF, Line SRP, *et al.* Bisphosphonates: pharmacokinetics, bioavailability, mechanisms of action, clinical applications in children, and effects on tooth development. *Environmental Toxicology and Pharmacology*. 42, 212–217 (2016).

25. Tenuta T, Monopoli MP, Kim J, *et al.* Elution of labile fluorescent dye from nanoparticles during biological use. *PLoS One*. 6(10), e25556 (2011).

26. Talamini L, Violatto MB, Cai Q, *et al.* Influence of size and shape on the anatomical distribution of endotoxin-free gold nanoparticles. *ACS Nano*. 11(6), 5519–5529 (2017).

27. D'Apolito R, Tomaiuolo G, Taraballi F, *et al.* Red blood cells affect the margination of microparticles in synthetic microcapillaries and intravital microcirculation as a function of their size and shape. *Journal of Controlled Release*. 217, 263–272 (2015). •

• This study explains how it is possible to promote particle contact and adhesion to the vesselwall.

28. Cremers S, Papapoulos S. Pharmacology of bisphosphonates. *Bone*. 49(1), 42–49 (2011).

29. Baroncelli GI, Bertelloni S. The use of bisphosphonates in pediatrics. *Hormone Research in Paediatrics*. 82(5), 290–302 (2014).

30. Lee D, Heo DN, Kim H-J, *et al.* Inhibition of osteoclast differentiation and bone resorption by bisphosphonate-conjugated gold nanoparticles. *Scientific Reports* [Internet]. 6, 27336 (2016). Available from: http://www.nature.com/articles/srep27336.

31. Cagel M, Grotz E, Bernabeu E, Moretton MA, Chiappetta DA. Doxorubicin: nanotechnological overviews from bench to bedside. *Drug Discovery Today*. 22(2), 270–281 (2017).

32. Guo X, Chang R-K, Hussain MA. Ion-exchange resins as drug delivery carriers. *Journal of Pharmaceutical Sciences*. 98(11), 3886–3902 (2009).

33. He X, Male KB, Nesterenko PN, Brabazon D, Paull B, Luong JHT. Adsorption and desorption of methylene blue on porous carbon monoliths and nanocrystalline cellulose. *ACS Applied Materials & Interfaces*. 5(17), 8796–8804 (2013).

34. Shi J, Votruba AR, Farokhzad OC, Langer R. Nanotechnology in drug delivery and tissue engineering: from discovery to applications. *Nano Lett.* 10(9), 3223–3230 (2010).

35. Lin N, Dufresne A. Surface chemistry, morphological analysis and properties of cellulose nanocrystals with gradiented sulfation degrees. *Nanoscale*. 6(10), 5384–5393 (2014).

36. Mondal S. Preparation, properties and applications of nanocellulosic materials. *Carbohydr Polym*. 163, 301–316 (2017).

~~For Table of Contents Only~~

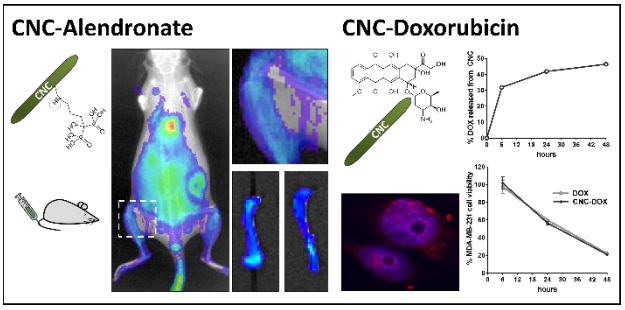

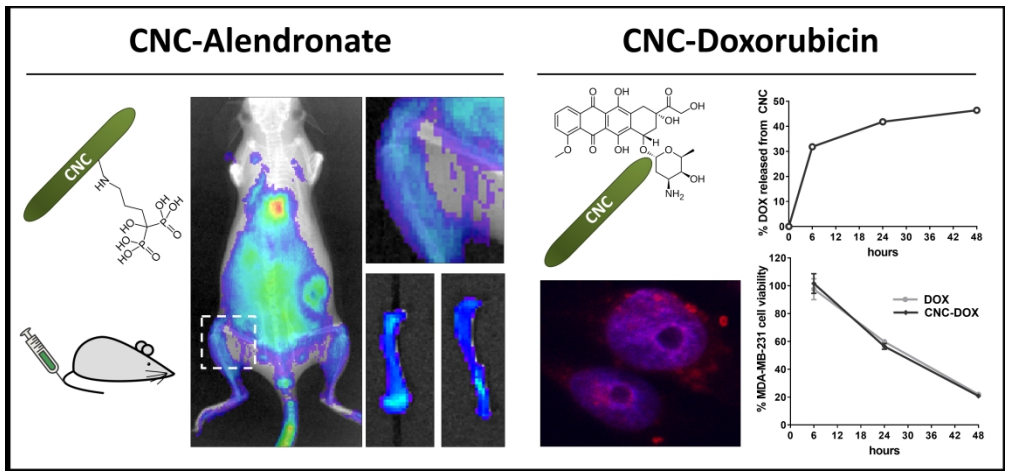

925x430mm (150 x 150 DPI)